

## **Distinct information conveyed to the olfactory bulb by feedforward input from the nose and feedback from the cortex**

Joseph D. Zak<sup>1,2,\*</sup>, Gautam Reddy<sup>3,4</sup>, Vaibhav Konanur<sup>1</sup> & Venkatesh N. Murthy<sup>4,5</sup>

1. Department of Biological Sciences, University of Illinois at Chicago, Chicago, IL 60607
2. Department of Psychology, University of Illinois at Chicago, Chicago, IL 60607
3. Physics & Informatics Laboratories, NTT Research, Inc., Sunnyvale, CA 94085
4. Center for Brain Science, Harvard University, Cambridge, MA 02138
5. Department of Molecular and Cellular Biology, Harvard University, Cambridge, MA 02138

\* Correspondence to [jdzak@uic.edu](mailto:jdzak@uic.edu)

### **Abstract**

Sensory systems are organized hierarchically, but feedback projections frequently disrupt this order. In the olfactory bulb (OB), cortical feedback projections numerically match sensory inputs. To unravel information carried by these two streams, we imaged the activity of olfactory sensory neurons (OSNs) and cortical axons in the mouse OB using calcium indicators, multiphoton microscopy, and diverse olfactory stimuli. Odorant mixtures of increasing complexity evoked progressively denser OSN activity, yet cortical feedback activity was of similar sparsity for all stimuli. Representations of complex mixtures were similar in OSNs but were decorrelated in cortical axons. While OSN responses to increasing odorant concentrations exhibited a sigmoidal relationship, cortical axonal responses were complex and non-monotonic, which could be explained by a model with activity-dependent feedback inhibition in the cortex. Our study indicates that early-stage olfactory circuits have access to both local feedforward signals and global, efficiently formatted information about odor scenes through cortical feedback.

## Introduction

Volatile odorants are sensed by olfactory sensory neurons (OSNs) in the main olfactory epithelium of mammals (Buck and Axel, 1991). Each OSN expresses only one odorant receptor (OR) type out of a large ensemble but can sense many ligands with different sensitivities (Malnic et al., 1999; Araneda et al., 2000). The large number of receptor types with broad selectivity is thought to underlie the combinatorial capacity of the olfactory system to sense a substantial number of odors in the natural world. Axons of OSNs expressing the same OR converge on glomeruli in the olfactory bulb (OB) (Ressler et al., 1994; Vassar et al., 1994; Mombaerts et al., 1996). This convergence is likely to help in signal averaging, and postsynaptic projection neurons called mitral/tufted (M/T) cells receive focused excitatory inputs from single glomeruli (Wachowiak and Shipley, 2006; Wilson and Mainen 2006). A complex network in the OB, which includes many types of inhibitory interneurons (Burton 2017), transforms the incoming odorant information before it is sent to downstream brain regions, including the piriform cortex (PC). An intriguing feature of the early olfactory system is the dense axonal feedback projections from olfactory cortical areas to the OB, which brings processed cortical information back to the earlier stages (Boyd et al., 2012; Markopoulos et al., 2012; Otazu et al., 2015; Pressler and Strowbridge, 2017). It is not fully clear how the feedforward information from the nose and feedback from the cortex interact in the OB.

The elaborate and often hierarchical organization of sensory systems is widely thought to help achieve efficient coding of information (Attneave 1954; Barlow 1961; Atick 1992). One way in which brains are thought to achieve efficient coding is by making responses of a neural population uncorrelated and of similar sparsity for a wide range of stimuli (Barlow 1961; Atick 1992; Bishop, 1995; Olshausen and Field, 1996; Vinje and Gallant 2000; Smith and Lewicki 2006). In the olfactory system, the repertoire of ORs is fixed in the genome and their responses to odorant stimuli may be inefficient - for example, certain odorants may activate many receptors and others may activate very few (Lin et al., 2006; Fletcher et al., 2009; Saito et al., 2009; Zak et al., 2020). To make the representation more efficient, circuits in different brain regions, including the OB and the PC may perform computations such as normalization or whitening (Wanner and Friedrich, 2020; Banerjee et al., 2015; Bolding and Franks 2017; Pashkovski et al., 2020). While circuits in the OB are likely to achieve some of the computational goals (Cleland and Linster, 2005), the PC is better situated for more global associations.

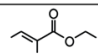
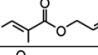
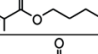
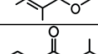
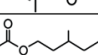
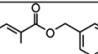
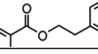
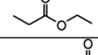
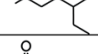
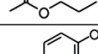
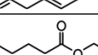
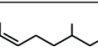
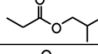
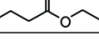


Principal cells in the PC integrate information from multiple glomerular channels in the OB, conveyed by M/T cells (Haberly and Price, 1977; Apicella et al., 2010; Sosulski et al., 2011). This information is then reformatted through recurrent excitatory and inhibitory circuitry in the PC, presumably to aid odorant perception. For example, the fraction of neurons in the PC responding to different monomolecular odorants is relatively constant (Stettler and Axel, 2009; Miura et al., 2012; Bolding and Franks, 2017; Iurilli and Datta, 2017), even though these odorants could activate very different densities of OSNs. Similarly, different concentrations of a given odorant activate a similar fraction of PC neurons (Stettler and Axel, 2009; Roland et al., 2017, Bolding and Franks, 2017, Bolding and Franks, 2018). Correlations in the representation of monomolecular odorants are also restructured in the PC (Pashkovski et al., 2020).

While previous studies point to normalization of olfactory responses in the PC (Penker et al., 2020), several key features remain unknown. For instance, even though the olfactory environment consists of a complex mixture of chemicals, we currently lack an understanding of how cortical neurons represent realistic odorant mixtures, which elicit complex interactions even in the OSNs (Rospars et al., 2008; Inagaki et al., 2020; Xu et al., 2020; Zak et al., 2020; Adefuin et al., 2022). Importantly, in the context of feedback, it is

unclear which of the different computations ascribed to the PC, related to odorant identity (Kadoshia and Wilson, 2006; Bolding and Franks, 2017), quality (Howard et al., 2009), attention (Zelano et al., 2005), and predictive coding (Zelano et al., 2011), are conveyed back to the OB.

In this study, we make use of a diverse set of olfactory stimuli to ask how their neural representation is transformed from the OSNs to feedback from the PC to the OB. We imaged the activity of mouse OSNs in the olfactory epithelium in response to pure odorants, as well as a wide variety of mixtures of odorants containing up to 12 components. We also imaged OSN responses to variations in odorant concentration over 4 orders of magnitude. We measured how expanding sensory input influences the activity of PC feedback by imaging its axonal projections to the OB. Our results reveal that cortical feedback axons bring back strongly normalized and decorrelated information about diverse odorant mixtures and concentrations to the OB, which can be combined with feedforward signals to influence M/T cell responses.

**Table 1**

Index	Name/Formula	Structure	CAS number	Molecular Weight (g/mol)	Standard Vapor Pressure (mmHg at 25°C)
1	Ethyl tiglate C <sub>7</sub> H <sub>12</sub> O <sub>2</sub>		5837-78-5	128.17	4.2690
2	Allyl tiglate C <sub>8</sub> H <sub>12</sub> O <sub>2</sub>		7493-71-2	140.18	1.2720
3	Hexyl tiglate C <sub>11</sub> H <sub>20</sub> O <sub>2</sub>		16930-96-4	184.27	0.0520
4	Methyl tiglate C <sub>6</sub> H <sub>10</sub> O <sub>2</sub>		6622-76-0	114.14	13.3790
5	Isopropyl tiglate C <sub>8</sub> H <sub>14</sub> O <sub>2</sub>		1733-25-1	142.20	1.8770
6	Citronellyl tiglate C <sub>15</sub> H <sub>26</sub> O <sub>2</sub>		24717-85-9	238.37	0.0036
7	Benzyl tiglate C <sub>12</sub> H <sub>14</sub> O <sub>2</sub>		37526-88-8	190.24	0.0010
8	Phenylethyl tiglate C <sub>13</sub> H <sub>16</sub> O <sub>2</sub>		55719-85-2	204.27	0.0010
9	Ethyl propionate C <sub>5</sub> H <sub>10</sub> O <sub>2</sub>		105-37-3	102.13	35.9000
10	2-Ethyl hexanal C <sub>8</sub> H <sub>16</sub> O		123-05-7	128.21	1.8000
11	Propyl acetate C <sub>5</sub> H <sub>10</sub> O <sub>2</sub>		109-60-4	102.13	35.2230
12	4-Allyl anisole C <sub>10</sub> H <sub>12</sub> O		140-67-0	148.20	0.1650
13	Ethyl Valerate C <sub>7</sub> H <sub>12</sub> O <sub>2</sub>		539-82-2	130.18	4.7450
14	Citronellal C <sub>10</sub> H <sub>18</sub> O		106-23-0	154.25	0.2800
15	Isobutyl propionate C <sub>7</sub> H <sub>14</sub> O <sub>2</sub>		540-42-1	130.18	6.4700
16	Allyl butyrate C <sub>7</sub> H <sub>12</sub> O <sub>2</sub>		2051-78-7	128.17	4.4430

**Table 1. Odorant information**

## Figure 1

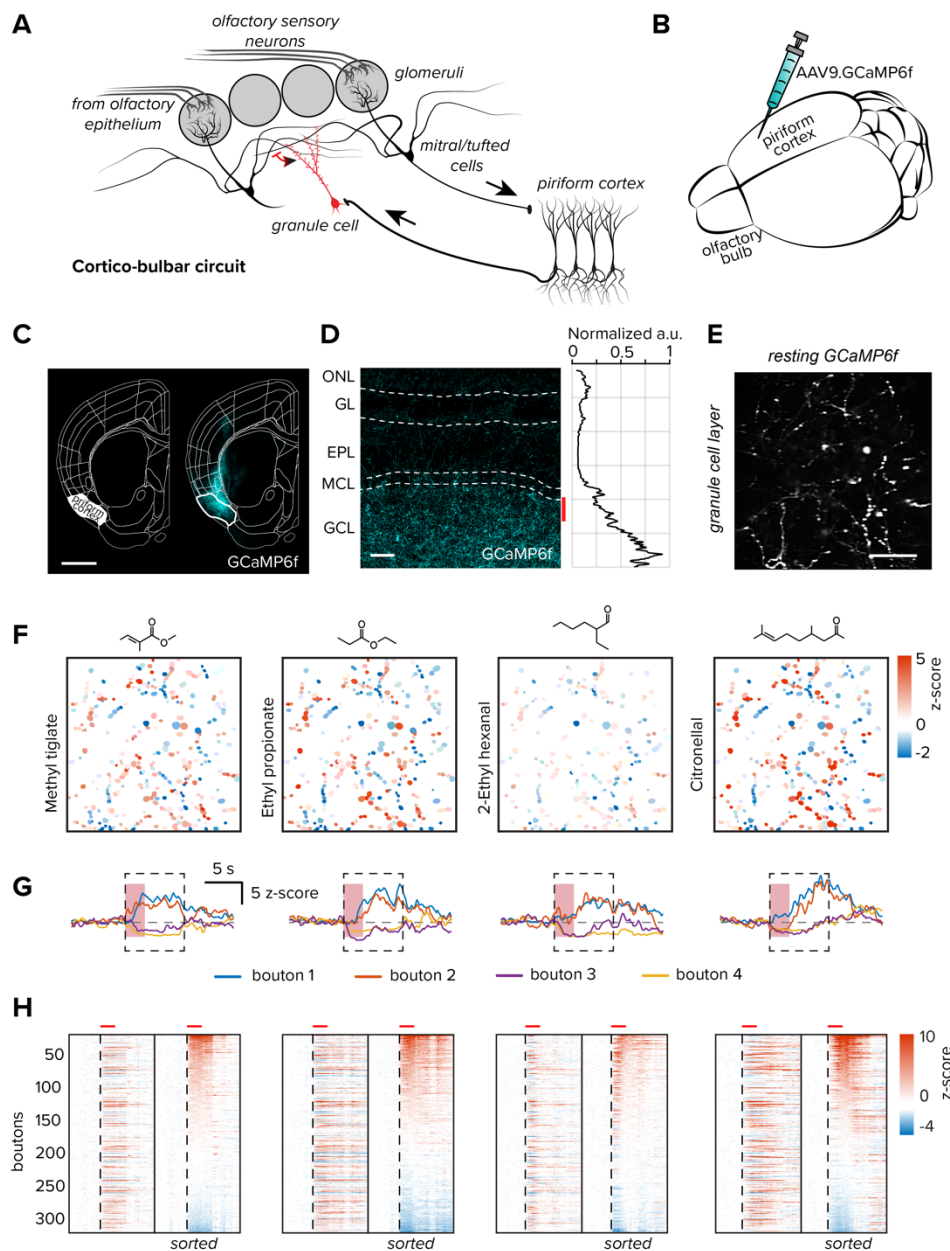


**Figure 1.** Viral expression of fluorescence indicators in the anterior PC.

**A.** Circuit schematic of cortico-bulbar connectivity. **B.** AAV9.GCaMP6f was injected bilaterally at two sites in the anterior region of the PC. **C.** Example coronal section of a mouse used in subsequent experiments GCaMP6f expression is targeted to the PC, scale bar = 1000  $\mu\text{m}$ . **D.** GCaMP6f expression in cortical projections to the OB. The red bar denotes the typical imaging depth for *in vivo* experiments, scale bar = 100  $\mu\text{m}$ . *Right*, the normalized fluorescence intensity in each layer of the OB. Olfactory nerve layer (ONL), glomerular layer (GL), external plexiform layer (EPL), mitral cell layer (MCL), and granule cell layer (GCL). **E.** *Left*, example image of GCaMP6f resting fluorescence of a typical imaging field, scale bar = 20  $\mu\text{m}$ . **F.** Responses to four selected odorants mapped onto ROI segments. **G.** Temporal modulation of GCaMP6f responses in four selected ROIs from each of the four odorants in *part F*. Response polarity is conserved across different stimuli. The red vertical shaded area denotes odorant delivery time. The dashed box indicates the response averaging window for subsequent analyses. **H.** Responses of each of the 341 boutons in the imaging field above to the same four odorants. *Left*, boutons are sorted by spatial location in the imaging field, *right*, traces are sorted by their mean response amplitude. The vertical dashed line denotes the odorant onset and the horizontal red bars above are the odorant duration.

## Results

### *Odorant tuning profiles of cortical projections to the OB*

Principal neurons in the PC integrate inputs from multiple glomeruli (**Figure 1A**) and can respond to odorant stimulation with either an increase or decrease in activity relative to their baseline activity (Otazu et al., 2015; Roland et al., 2017; Bolding and Franks, 2017). We began our study by systematically measuring the responses of cortical feedback axons in the OB of awake mice to a panel of monomolecular odorants.

A cocktail of two viruses was injected into the anterior portion of the PC (see Methods) to drive the expression of the calcium indicator GCaMP6f (**Figure 1B**) and the fluorescent marker tdTomato (see **Supplemental Figure 1**), which was used to identify regions containing infected projections and for motion artifacts compensation. A *post hoc* analysis revealed dense indicator expression in the somata of neurons in layer 2/3 of the PC (**Figure 1C**), as well as their axonal projections in the granule cell layer of the OB (**Figure 1D**). Projections could also be observed to reach the glomerular layer of the OB, although at lower densities.

In living mice imaged through cranial windows, we observed dense indicator expression at the interface between the external plexiform and granule cell layers (**Figure 1E**). To measure functional responses, we selected a standardized odorant panel that has previously been used in our laboratory for both behavioral and physiological studies (Rokni et al., 2014; Zak et al., 2020) (**Table 1**). Odorants were delivered in a pseudorandom order and the evoked responses were measured in individual axonal boutons by generating ROI masks from spatiotemporal correlograms (Pnevmatikakis 2018; Giovannucci et al., 2019; **Figure 1F**). Within individual imaging fields, enhanced and suppressed bouton responses were spatially distributed throughout the area imaged and their response kinetics varied by odorant identity (**Figure 1F-H**).

In our characterization of odorant tuning profiles of cortical feedback, we collected data from 832 boutons in nine imaging fields from six mice. Exemplar odorant response characteristics are shown in **Figure 1**. For all bouton-odorant pairs that were significantly stimulus-modulated, response polarities were typically conserved over the odorant panel (**Figure 2A**). Individual bouton responses were generally either enhanced or suppressed across the odorant panel, and a smaller fraction showed mixed responses (37.5% enhanced, 38.0% suppressed, 24.5% mixed). These proportions are significantly different from chance, which would be  $6.5 \pm 0.6\%$  enhanced,  $11.7 \pm 0.3\%$  suppressed and  $81.3 \pm 1.0\%$  mixed, if odor-bouton responses are independently drawn from the distribution shown in **Figure 2B** (see Methods; deviations are 99% confidence intervals). Our findings are consistent with other studies which report that response polarity is conserved between stimuli within the PC and descending axons terminating within the OB (Otazu et al., 2015; Bolding and Franks, 2017; Roland et al., 2017).

Most boutons did not respond to any particular stimulus ( $72.2 \pm 1.3\%$  unresponsive,  $n = 16$  odorants; **Figure 2B**). However, of the boutons that were odorant-modulated, suppressed responses were more frequent than enhanced responses ( $15.4 \pm 0.9\%$  suppressed vs.  $12.4 \pm 0.9\%$  enhanced,  $n = 16$  odorants,  $P = 0.038$ , sign-rank test; **Figure 2B**). We next considered the tuning widths of individual boutons by estimating the number of effective odorants, that is, those that generated a response significantly above or below baseline activity (see Methods). Boutons that were suppressed by odorant stimulation were more broadly tuned than those that were enhanced ( $3.9 \pm 0.2$  effective odorants for suppressed boutons and  $3.2 \pm 0.2$  effective odorants for enhanced boutons;  $n = 16$  odorants;  $P = 0.009$ ; rank sum test; **Figure 2C**).

**Figure 2**

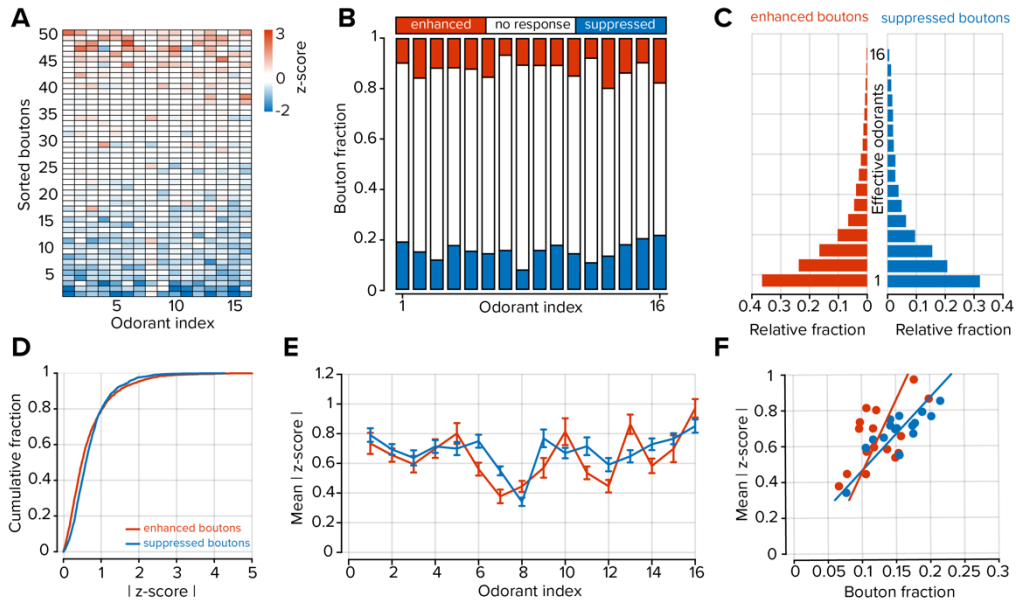


**Figure 2.** Odorant tuning properties of cortical projections to the OB.

**A.** Odorant tuning profiles of 50 randomly selected boutons selected from all imaging fields. Boutons are sorted by their mean response amplitude across all odorants. **B.** Fraction of responding boutons for each odorant. **C.** Distributions of effective odorants for boutons that showed net enhanced ( $3.2 \pm 0.1$  odorants) or suppressed ( $3.9 \pm 0.2$  odorants) responses ( $n = 16$  odorants;  $P = 0.009$ ; rank sum test). **D.** Cumulative distributions of all stimulus-modulated responses at all odorants for enhanced and suppressed boutons ( $P < 0.001$ ; Kolmogorov-Smirnov test). **E.** Mean response of all significantly modulated boutons separated by response polarity for each odorant ( $p = 0.39$ ; Kruskal-Wallis test), error bars represent standard error of the mean (s.e.m). **F.** Scatter plot of the relationship between response density (bouton fraction) and the mean response amplitude for each odorant separated by response polarity ( $r = 0.81$  for suppressed boutons  $P < 0.001$ ;  $r = 0.57$  for enhanced boutons,  $P = 0.021$ ).

Suppressed boutons responded more strongly to odorant stimulation than enhanced boutons ( $0.67 \pm 0.01$  z-score for enhanced boutons,  $n = 1652$  bouton-odorant pairs;  $0.71 \pm 0.01$  z-score for suppressed boutons,  $n = 2046$  bouton-odorant pairs;  $P < 0.001$ ; Kolmogorov-Smirnov test; **Figure 2D**); however, when considering each odorant, the average population responses of enhanced boutons were similar to suppressed boutons ( $P = 0.39$ ; Kruskal-Wallis test; **Figure 2E**). In both suppressed and enhanced boutons there was a significant positive relationship between the fraction of activated elements and their mean activity ( $r = 0.81$  for suppressed boutons  $P < 0.001$ ;  $r = 0.57$  for enhanced boutons,  $P = 0.021$ ; **Figure 2F**). Overall, in response to a monomolecular odorant, cortical feedback axons exhibited a balanced profile of activation and suppression that was statistically similar for all stimuli.

#### *Cortical feedback boutons are more broadly tuned than individual feedforward input to the OB*

To estimate the relative sparsity of bouton responses, we compared their properties to those of OSNs using the same odorant panel. In OMP-GCaMP3 mice, we used a bone-thinning procedure to gain optical access to individual OSNs within the olfactory epithelium (**Figure 3A**; Inagaki et al., 2020; Zak et al., 2020; Zak, 2022). We then delivered the same 16 odorants as we did for experiments imaging feedback projections to the OB.

Cortical neurons are expected to be more broadly tuned than sensory cells given the convergent circuit architecture of bulbar inputs to the PC (Apicella et al., 2010; Davison and Ehlers, 2011; Vicente and Mainen, 2011). Our data, which makes use of the same odorants to stimulate both OSNs and cortical projections to the OB indeed supports this expectation. We found that OSNs responded to  $3.15 \pm 0.15$  odorants in our panel, while feedback projections responded to  $4.45 \pm 0.13$  odorants ( $n = 377$  OSNs, 832 boutons;  $P < 0.001$ ; rank-sum test). However, somewhat unexpectedly, cortical projections are on average only sensitive to only  $\sim 1.5$  more odorants out of 16, far less than the estimated convergence of  $\sim 200$  glomeruli per cortical neuron (Vicente and Mainen, 201; Sheppard, 2004).

To visualize the selectivity of individual OSNs and boutons to each of the stimuli we first rank-ordered the absolute value of responses to all 16 odorants and normalized them to the largest response (mean responses across all odorants, OSNs =  $0.26 \pm 0.06$ , boutons =  $0.38 \pm 0.07$ ; Comparison of ranked distributions,  $P < 0.001$ ; sign rank test; **Figure 3B**). Measurements of lifetime sparseness (see *Methods*) also indicated an increased turning breadth in cortical projections compared to OSNs (mean lifetime sparseness,  $0.46 \pm 0.004$  in OSNs and  $0.65 \pm 0.002$  in boutons;  $P < 0.001$ ; Kolmogorov-Smirnov test; **Figure 3D**). However, when normalized, uniformly weak responses across a population could conflate relative population activities. To address this, we also measured population sparseness. Using this metric we found that bouton responses were indeed denser than in OSNs ( $0.49 \pm 0.01$  boutons,  $0.37 \pm 0.04$  OSNs;  $P = 0.013$ ; sign rank test;  $n = 16$  odorants **Figure 3C,E**), and these measurements were consistent across trials using the same odorants (**Figure 3G**).

The responses of boutons to odorants were measured in awake mice, but OSN responses were acquired in anesthetized mice. To compare these two populations under similar conditions, we anesthetized animals with a cocktail of ketamine and xylazine and measured cortical feedback responses to the same panel of odorants (**Supplemental Figure 2**). Under anesthetized conditions, feedback boutons were similarly tuned compared to awake animals, but the density of responses per odorant was reduced (**Supplemental Figure 2D-F**). Despite the decreased density of response in anesthetized animals, we did not observe a systematic relationship between odorant tuning in anesthetized boutons and OSNs (**Supplemental Figure 2F,J**).

We next estimated the representational similarity (see *Methods*) between pairs of odorants in our panel for OSNs and cortical boutons in the OB. In OSNs, a subset of the odorants showed similarity with other odorants in the panel and relationships could be determined using hierarchical clustering of odorant-odorant correlations (**Figure 3H, left**). The odorant representations were well-preserved between trials of the same odorant ( $0.78 \pm 0.03$  mean correlation in OSNs;  $n = 16$  odorants; **Figure 3I**). However, in cortical projections, odorant responses in awake mice were more variable between trials ( $0.53 \pm 0.02$  mean correlation  $P < 0.001$ , sign rank test; **Figure 3I**), and the pairwise odorant relationships determined from OSNs did not map onto bouton pairwise odorant similarities (boutons to OSNs  $r = -0.03$ ;  $P = 0.59$ ; **Figure 3J**). Interestingly, in anesthetized animals, we found a restructuring of odorant-odorant relationships and decreased trial variability (**Supplemental Figure 2H,J**), yet there was no apparent relationship to representations in OSNs. The increased representational similarity between odorants in anesthetized animals could be due to reduced effective inhibition in the recurrent circuitry in the OB or the PC (Rinberg et al., 2006; Kato et al., 2012; Bolding and Franks, 2020). These data indicate cortical feedback axons are more broadly tuned to monomolecular odorants than OSNs, but have significantly decorrelated patterns of responses to different odorants than OSNs.

### Figure 3

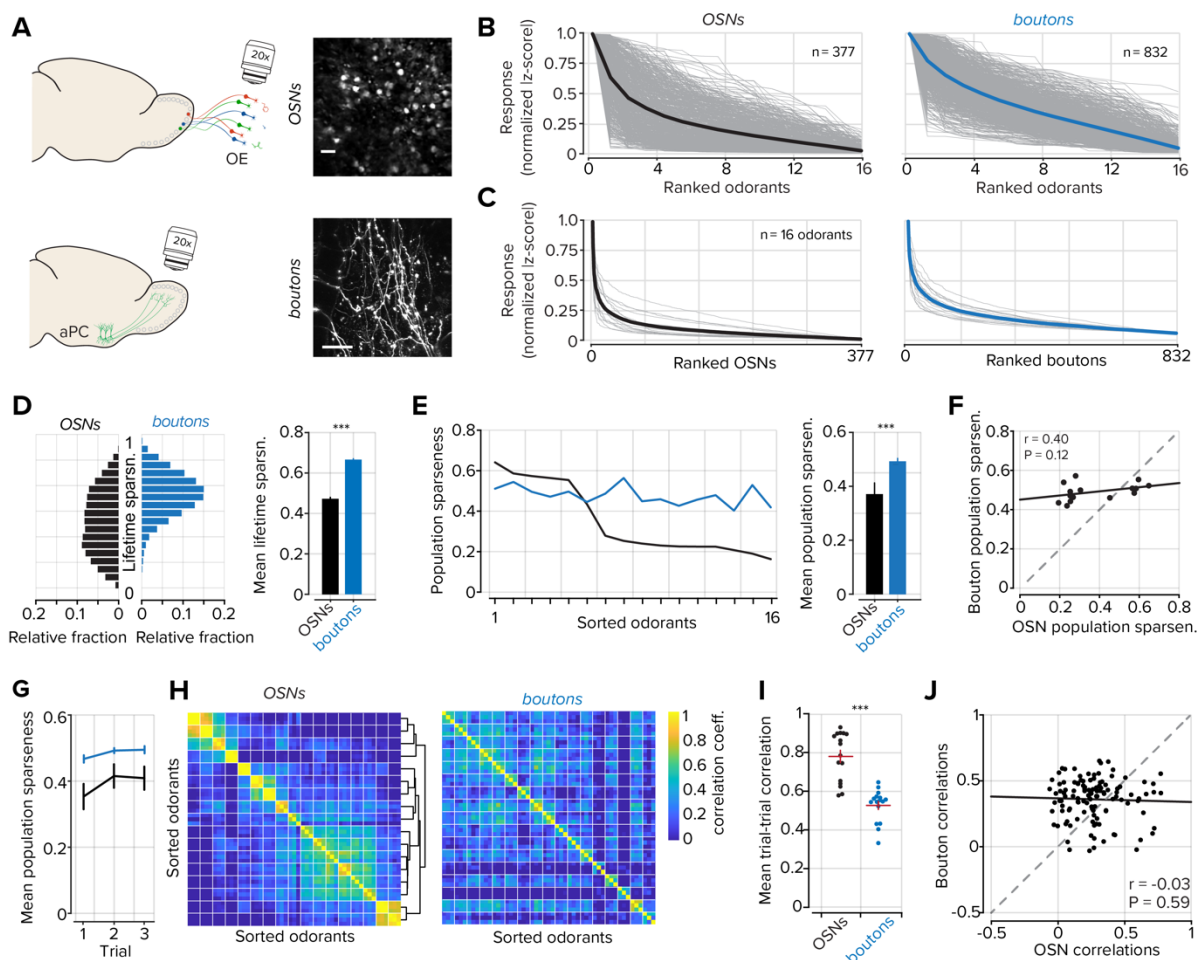


**Figure 3. Odorant representations in feedforward and feedback pathways to the OB.**

**A.** Top, example images of GCaMP3 expressing OSNs in the olfactory epithelium, scale bar = 20  $\mu$ m. Bottom, GCaMP6f expressing cortical projections to the OB, scale bar = 20  $\mu$ m. **B.** Normalized and ranked responses to 16 odorants in OSNs (black; n = 377) and cortical projections to the OB (blue, n = 832). Each tuning curve is independently sorted and ranked. Gray lines represent individual ROIs and thick colored lines represent the mean of all ROIs. **C.** Normalized and ranked responses of each OSN and cortical bouton for each of the 16 odorants. Gray lines represent individual odorants and thick colored lines represent the mean of all odorants. **D.** Left, Distributions of lifetime sparseness measured in OSNs (black) and cortical projections (blue). Right, mean lifetime sparseness was measured in OSNs and cortical projections. Error bars represent s.e.m. **E.** Left, population sparseness for each of 16 odorants sorted to OSN values. Right, mean population sparseness for all odorants. Error bars represent s.e.m. **F.** Scatter plot of the relationship between OSN population sparseness and bouton population sparseness.  $r = 0.40$ ,  $P = 0.12$ . **G.** Mean population sparseness for each of three trials. Error bars represent s.e.m. **H.** Odorant-odorant correlations in OSNs and boutons. Individual odorants are bounded by white lines and each odorant contains three trials. Hierarchical clustering was used to group similar odorants in OSNs and the clusters were then used to group datasets in boutons, see *Supplemental Figure 2* for odorant labels. **I.** Variability within trials of the same odorants in OSNs and boutons. The horizontal red bar denotes the mean and the vertical red bars represent s.e.m. **J.** Scatter plot of the relationship between odorant-odorant correlations in OSNs and boutons.  $r = -0.03$ ,  $P = 0.59$ . \*\*\* denotes  $P < 0.001$ .



## *Responses to complex odorant mixtures are normalized in the PC*

The density of OSN activation can be systematically varied by delivering mixtures of monomolecular odorants with an increasing number of components (Zak et al 2020). We devised a panel of 84 mixtures derived from the 16 monomolecular odorants that were used earlier in our study (see **Supplemental Table 1**). The mixtures varied in complexity, contained 2, 4, 8, or 12 unique components, and were delivered to mice in pseudorandom order.

In OSNs, the activity and density of responses scaled, on average, with the number of odorant components within a mixture (**Figure 4Ai,Bi**). However, despite a general increase in OSN activity with mixture complexity, the relationship is sublinear such that progressive increases in mixture complexity lead to increases in OSN activity at a diminishing rate (Mathis et al., 2016; Xu et al., 2020; Zak et al., 2020). We also identified a subpopulation of OSNs that responded to odorant mixtures with decreases in activity (Inagaki et al., 2020; **Figure 4Ai, right**) and included these responses in our subsequent analyses when deviations from baseline activity met the inclusion criteria (see *Methods*).

We delivered the same panel of odorant mixtures to awake mice (three animals, five imaging fields), in the same order while imaging cortical projections to the OB. The mixture response distributions measured in the cortical feedback boutons had no relationship to the number of components in an odorant mixture and the mean activity of all activated boutons was similar at each mixture size (**Figure 4Aii-Bii**). We next visualized the selectivity of individual OSNs and boutons to the range of mixture stimuli (**Figure 4C**). For each element, we rank-ordered the absolute value of responses to all 100 stimuli and normalized them to the largest response. The rank-ordered bouton responses were sparser than those of OSNs (**Figure 4C**; comparison of mean distributions,  $P < 0.001$ ; sign rank test). The width of these "tuning curves" can also be characterized by measuring the lifetime sparseness (**Figure 4D**). The lifetime sparseness of OSNs was strongly related to the mixture size – OSNs responded to more mixtures of a particular size as the size increased ( $P < 0.001$ , one-way ANOVA). While bouton lifetime sparseness did not scale with the number of components in a given mixture and was constant regardless of mixture size (**Figure 4D, right**).

We next considered the population responses for each odorant mixture by rank-ordering them for each of the 100 mixture stimuli. While there was no difference between feedback boutons and OSNs in the ranked mean activity of all of the mixtures (**Figure 4E**; Comparison of mean distributions,  $P = 0.22$  Kolmogorov-Smirnov test), the distributions of individual odorant mixtures differed, with OSNs being more variable than boutons. To estimate the spread of the mixture activity distributions, we measured its difference from the mean curve for each odorant mixture, averaging over the entire curve. Using this distance metric, we found that the population tuning for the 100 stimuli was significantly variable for OSNs, but was highly similar for boutons (**Figure 4E**; OSN distance =  $0.11 \pm 0.01$ , bouton distance =  $0.03 \pm 0.002$  in boutons;  $P < 0.001$ ; Kolmogorov-Smirnov test). The stimulus tuning of each OSN or bouton can also be calculated by measuring population sparseness. For each of the mixture sizes, the mean population sparseness of OSNs and boutons were similar (**Figure 4F**), yet when considering all mixtures OSNs had more variance in the sparsity of their responses ( $P < 0.001$ ; F-test). Together, these data indicate that diverse stimuli that elicit highly divergent response sparsity in the OSNs are strongly equalized in cortical feedback axons.

**Figure 4**

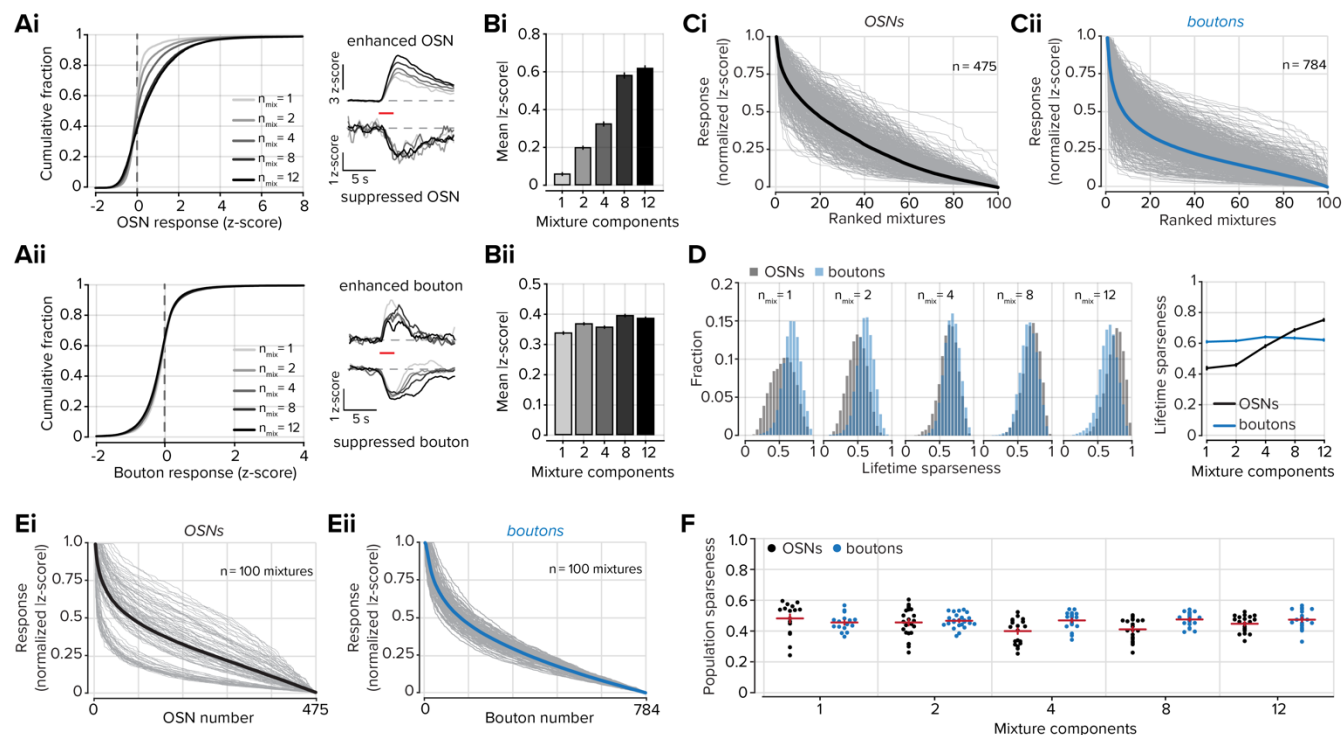


**Figure 4.** Odorant mixtures are normalized by the PC.

**Ai-ii.** Left, distributions of OSN or bouton responses to odorant mixtures of increasing size. Grayscale shade corresponds to the mixture size. Right, Example GCaMP responses of OSNs and boutons show enhanced or suppressed responses to odorant mixtures. Traces are averages of all significant responses of a given mixture size. Grayscale shade corresponds to the distributions on the left. The horizontal red bar indicates odorant delivery. **Bi-ii.** Mean activity at each mixture complexity in OSNs or boutons. **Ci-ii.** Normalized and ranked responses of 100 odorant mixtures in OSNs (black;  $n = 475$ ) and cortical projections in awake mice (blue,  $n = 784$ ). Each tuning curve is independently sorted and ranked. Gray lines represent individual ROIs and thick colored lines represent the mean of all ROIs. **D.** Left, Distributions of lifetime sparseness for each group of mixtures of a given size. Right, summary data of mean lifetime sparseness at each mixture size. Error bars represent s.e.m. **E.** Normalized and ranked responses of each OSN and bouton for each of the 100 mixtures. Gray lines represent individual odorant mixtures and thick colored lines represent the mean of all mixtures. **F.** Population sparseness for each mixture of a given size. The horizontal red bar denotes the mean and the vertical red bars represent s.e.m.

### Representational similarity for mixture stimuli

We next compared the representational similarity of odorant mixtures in feedforward and feedback inputs to the OB. In OSNs, the responses to mixtures became more similar as the number of odorants in a mixture increased (**Figure 5A**), while in feedback projections, the representational similarity did not vary systematically with the mixture size (**Figure 5B**). For each mixture, we then compared the relationship of pairwise mixture-mixture correlations between boutons and OSNs. Although there was a significant relationship between correlations found between OSNs and boutons, the slope of the regression was shallow and reflected the relatively narrower range of mixture-mixture correlations found in boutons ( $r = 0.12$ ;  $P < 0.001$ ; **Figure 5C**).

To be certain that we did not introduce a sampling bias to our analysis by selecting an uneven number of boutons from different axons, we also analyzed non-contiguous ROIs from each imaging field (See Methods). Our results did not change when we considered axon segments rather than boutons, and the representational similarity did not vary with the mixture size (**Supplementary Figure 3**). Furthermore, boutons are small structures and comprise fewer pixels than OSNs. To address the possibility that the small number of pixels sampled from each bouton obscured relationships between odorant mixtures, we subsampled OSN ROIs to match boutons (**Supplementary Figure 4**). Even when a single pixel was drawn from each OSN ROI, the structure in the mixture-mixture relationships remained, indicating the differences between OSNs and boutons are not due to the size of the analyzed regions.

For the two largest mixture sizes, we then compared the representational similarity in OSNs and feedback projections between highly overlapping mixtures, those that shared  $\geq 75\%$  of their components, and other mixtures that had  $< 75\%$  overlap. In OSNs, mixtures that shared  $\geq 75\%$  of their components had on average more similar representations than mixtures that shared fewer components ( $0.77 \pm 0.01$  mean correlation when mixture overlap  $\geq 75\%$ ,  $n = 152$  mixture pairs  $0.63 \pm 0.01$  mean correlation when mixture overlap  $< 75\%$ ,  $n = 228$  mixture pairs;  $P < 0.001$ , Kolmogorov-Smirnov test; **Figure 5Di**). In contrast, there was no difference in the mean correlation in cortical projections when mixtures contained greater or less than 75% overlap ( $0.48 \pm 0.01$  mean correlation when mixture overlap  $\geq 75\%$ ,  $0.46 \pm 0.01$  mean correlation when mixture overlap  $< 75\%$ ;  $P = 0.06$ , Kolmogorov-Smirnov test; **Figure 5Dii**). These results indicate the representations of different mixtures become equally distinct from each other in cortical feedback, independent of mixture complexity.

**Figure 5**

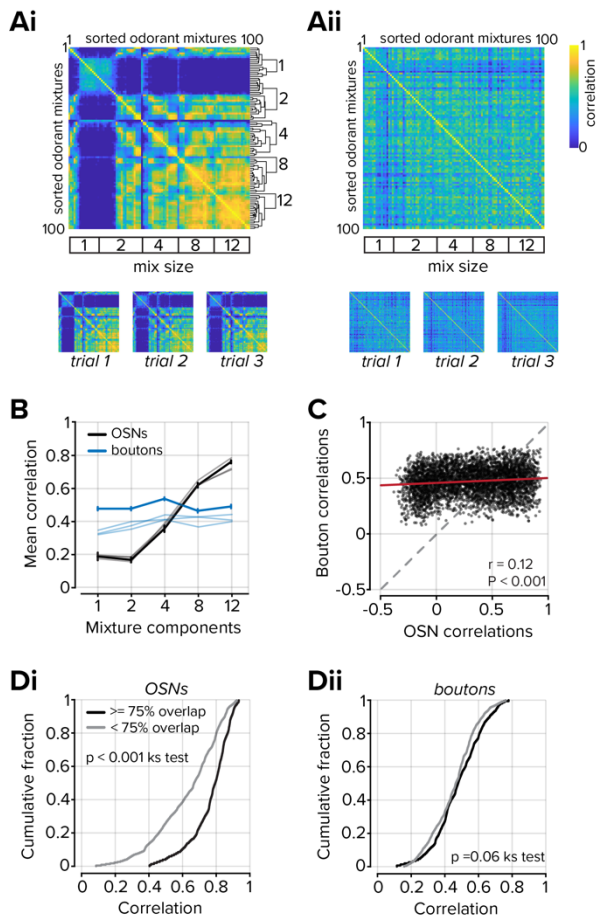


**Figure 5. Representations of odorant mixtures in OSNs and the PC.**

**A.** Correlation matrices of mixture-mixture relationships in OSNs (**Ai**) and boutons (**Aii**). Hierarchical clustering was used to group mixtures at each mixture size using OSNs. The clusters were then used to sort the bouton dataset. *Bottom*, Correlation matrices were obtained from three independent trials, showing similarity to the mean of all trials above. **B.** Plot of the mean correlation of all mixtures of a given complexity. Data from individual trials are plotted as shaded lines. Error bars represent s.e.m. **C.** Scatter plot of the relationship between mixture-mixture correlations in OSNs and boutons for each mixture size. **D.** Mixtures were divided into two groups based on mixture overlap using a threshold of 75%. **Di.** The OSN population activity was more correlated when mixtures shared  $\geq 75\%$  ( $P < 0.001$ , Kolmogorov-Smirnov test) **Dii.** In boutons, no difference was observed ( $P = 0.06$ , Kolmogorov-Smirnov test).

## *Nonmonotonic representations of odorant concentration in PC neurons*

The activity of sensory cells at the periphery typically scales with stimulus intensity (Rospars et al., 2000; Wen et al., 2009; Teng et al., 2019). To corroborate this expectation, we imaged OSNs both at their somata in the OE and their axon terminals in the glomerular layer of the OB (**Figure 6Ai**) in response to increasing odorant concentrations (see **Table 1**, index 4 for odorant properties; **Supplementary Figure 5** for additional odorant). In OSNs, population activity scaled with odorant concentration (**Figure 6Bi**). Furthermore, as the odorant concentration increased, representations of the odorants became more similar at adjacent concentrations, approaching the similarity of responses between trials at the same concentration (**Figure 6Ci,D**).

How do cortical projections to the OB respond to the same odorants at increasing concentrations? There is clear evidence of concentration invariance in neurons in the PC (Roland et al., 2017; Bolding and Franks, 2018), but, whether this invariance is reflected in back projections to the OB has not been investigated using a sufficiently large concentration range that is adequately sampled with intermediate points (some earlier studies used less than 2-fold changes in concentrations). We repeated the same experiment using nearly identical odorant concentrations while imaging cortical feedback activity in the OB (**Figure 6Aii-Cii**).

Bouton responses to increasing odorant concentrations could not be fitted with a sigmoidal function and lacked characteristic monotonic responses that were observed in OSNs (**Figure 6Ai vs. 6Aii**). At the population level, these response properties are consistent with concentration-invariant odorant coding in the PC. However, many individual boutons displayed a clear preference for select and non-overlapping ranges of concentrations (**Figure 6Aii, right**). Therefore, the information inherited from the PC in the OB may on average reflect concentration invariance, yet, at a more granular level, the PC may provide information on select concentrations. This observation substantiates other studies of odorant-concentration coding in feedback projections to the OB which found that non-monotonic concentration dependence was prevalent (Otazu et al., 2015).

Like in the OSNs, the representational similarity of odorants measured in boutons increased as a function of concentration (**Figure 6Cii**). However, trial-to-trial variability within a concentration block was greater in boutons than in OSNs (**Figure 6D, left**). The increase in similarity between trials at high concentrations could reflect an increasing number of active cells. In the OSNs, the proportion of active cells, measured through population sparseness, had a strong relationship to odorant concentration and plateaued at the highest concentrations (**Figure 6E**). However, the proportion of activated boutons did not scale with odorant concentration and was similar regardless of odorant concentration ( $0.50 \pm 0.03$  mean population sparseness in boutons,  $0.18 \pm 0.05$  mean population sparseness in OSNs;  $n = 8$  concentrations;  $P = 0.008$ ; sign rank test). We then considered the tuning of each bouton or OSN to the discrete points on the concentration axis. On average, boutons were more widely tuned, as measured by lifetime sparseness, than were OSNs. While some OSNs displayed broad tuning, within the range of tuning seen for cortical boutons, another population was more selective and responded to only a single or few concentration points at the highest end of the concentration range (**Figure 6F**;  $0.69 \pm 0.01$  mean lifetime sparseness in boutons,  $n = 1125$ ;  $0.51 \pm 0.01$  mean lifetime sparseness in OSNs;  $n = 1185$ ;  $P < 0.001$ ; Kolmogorov-Smirnov test). Our data indicate that cortical feedback axons bring complex, non-monotonic information to the OB with increasing concentration of individual odors.

## Figure 6

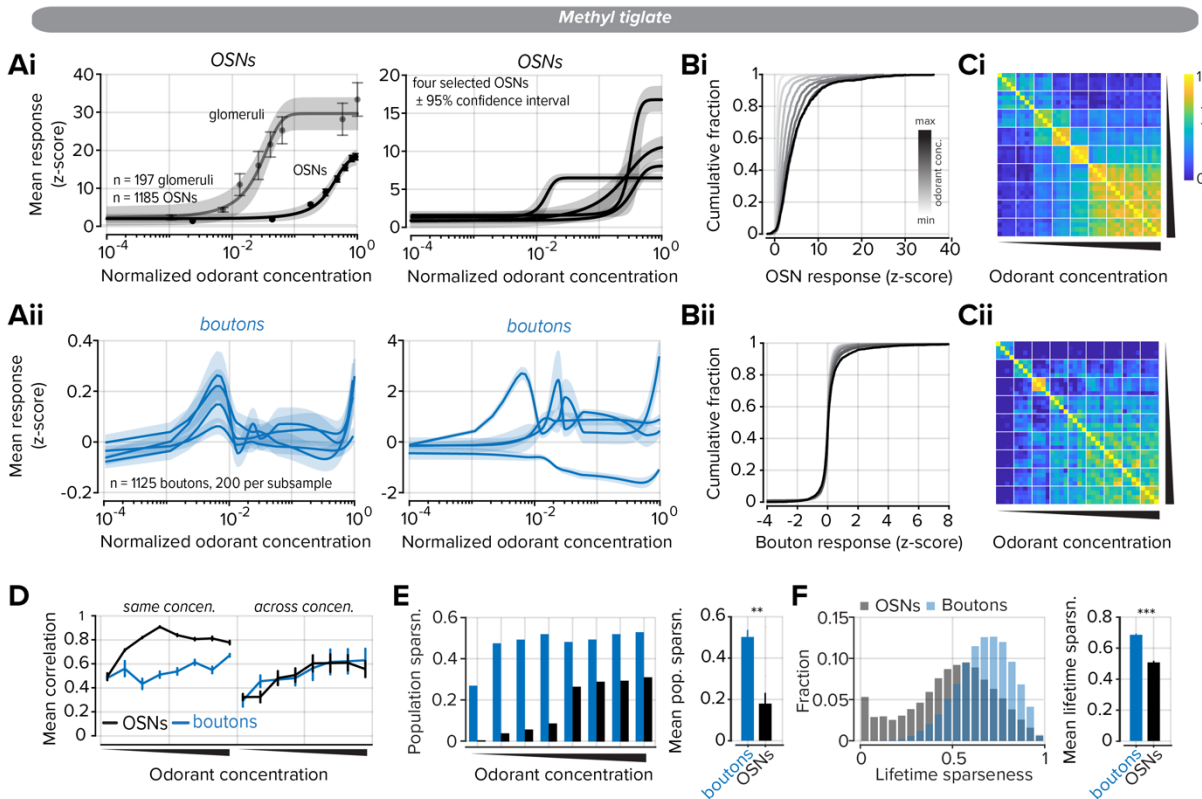


**Figure 6.** Odorant responses in cortical projections to the OB are nonmonotonic.

**Ai.** *Left*, odorant concentration responses were measured in OSN somata in the OE and their axon terminals within the glomerular layer. Error expressed as s.e.m on individual data points and shaded 95% confidence interval for the sigmoidal fit. *Right*, four example OSN responses. **Aii.** *Left*, odorant concentration responses were measured in cortical boutons in the OB. Four traces show subsamples selected from 200 boutons each. Data were fitted with an Akima piecewise cubic Hermite interpolation. The shaded area represents the confidence interval. *Right*, four examples of individual bouton responses. **B.** Distributions of OSN (**Bi**) and bouton (**Bii**) responses to increasing odorant concentration. Color shade corresponds to the odorant concentration. **C.** Correlation matrix of odorant responses (each pixel is the pairwise correlation of the corresponding row and column elements) to increasing odorant concentration in OSNs (**Ci**) and boutons (**Cii**). White lines bound concentrations and each concentration block contains four trials. **D.** *Left*, OSN, and bouton correlations between trials at the same odorant concentration trials. *Right*, OSN and bouton correlations across concentrations. **E.** *Left*, population sparseness at each odorant concentration. *Right*, summary data of mean population sparseness for all concentrations. Error bars represent s.e.m. **F.** *Left*, Distributions of lifetime sparseness measured for all concentrations. *Right*, summary data of mean lifetime sparseness. Error bars represent s.e.m. \*\* denotes  $P < 0.01$ , \*\*\* denotes  $P < 0.001$ .

### *Integrated activity-dependent inhibition explains non-monotonic concentration dependence in the PC.*

What accounts for the non-monotonic concentration dependence observed in the cortical projections to the OB? To answer this question, we developed a minimal model of bulb-to-cortex circuit elements that incorporated global, activity-dependent inhibition within the PC (Bekkers and Suzuki, 2013) that can account for our experimental observations (**Figure 7A**).

Specifically, we consider a sigmoidal dose-response model for the OSNs where an odorant binds to different OSN types with a broad range of affinities and upon binding activates a sparse subset of these OSNs (**Figure 7B**). The response from olfactory sensory neurons is transformed linearly to the PC via the mitral cell population. This assumption about mitral cells is reasonable since published data indicate that mitral cell responses are gain-modulated by circuits in the OB, but still exhibit monotonic responses to increasing concentrations of odor stimuli (Banerjee et al., 2015). Our PC model consists of two populations of cells: one population that receives excitatory input from the OB and projects back to the OB, and a second population of inhibitory interneurons that mediate global, non-specific inhibition. Inhibitory activity of the latter population is triggered when the summed activity of the former population exceeds a threshold. Below this threshold, the activity of the principal cells (and by extension, the feedback axons) increases monotonically with concentration until global inhibition kicks in, at which point their activity decreases (**Figure 7C**). At sufficiently high concentrations, the excitatory input overcomes the inhibition, which leads to a second monotonic phase. Note that even though the dose-response curves of individual cells are non-monotonic, the delay before inhibition acts implies that response latency decreases monotonically with concentration (**Figure 7D**), as observed empirically (Bolding and Franks, 2017).

**Figure 7**

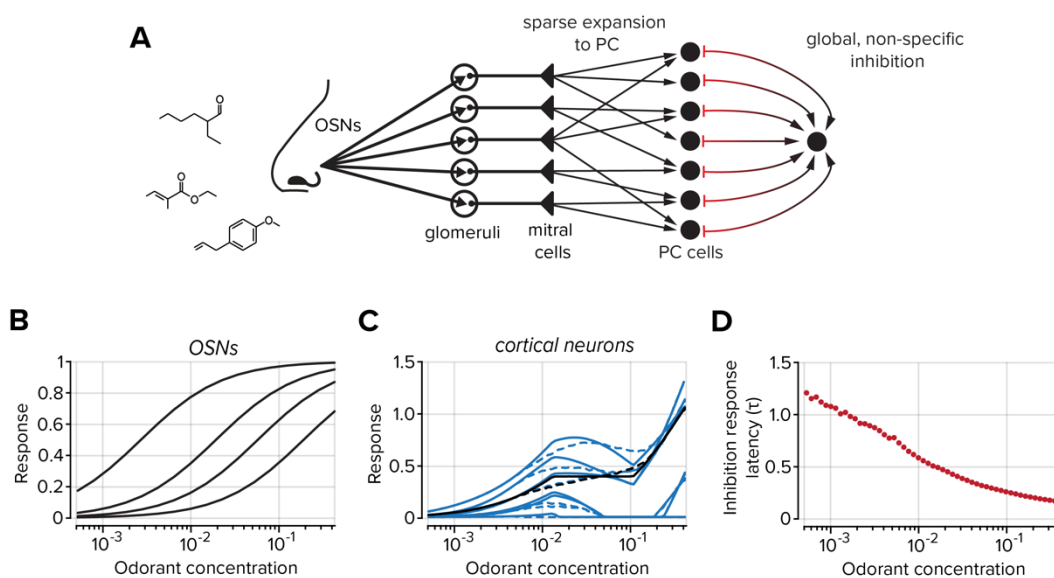


**Figure 7.** A model of bulbo-cortical connectivity produces non-monotonic concentration dependence in cortical neurons.

**A.** Model schematic including sparse expansion from the OB to the PC and global, non-specific inhibition within the PC. **B.** The response of olfactory sensory neurons is monotonic with odorant concentration, as empirically observed in **Figure 6**. Each black line represents the activity of an individual OSN. **C.** The activity of the feedback axons increases monotonically with concentration until global inhibition is activated, at which point axon activity decreases, then recovers. See **Figure 6Aii**. Solid and dashed blue lines show dose-response curves for five representative cortical neurons in models with identical and heterogeneous inhibitory interneurons respectively (see *Methods* for details on interneuron activity). Solid and dashed black lines show the average dose-response curves across all cortical neurons for these two models. **D.** The response latency (in units of the membrane time constant) of cortical neurons decreases monotonically with concentration despite the non-monotonic dependence on odorant concentration.

## Discussion

The OB receives dense axonal input not only from the sensory periphery but also cortical and associational areas of the brain. The stimulus tuning and response properties of peripheral input to the OB have been extensively described; however, less progress has been made on descending inputs to the OB, and how they reflect the integrative and convergent architecture of the OB to PC circuitry. In our study, we systematically probed the tuning properties of cortical projections to the OB to understand how expanding sensory inputs are processed by the PC and represented in its descending inputs to the OB. We changed the density of OSN activity in two different ways - cumulative recruitment with increasing concentration, and a more randomized increase with increased mixture complexity. We find that cortical axons bring back information to the OB that is highly equalized over a wide variety of stimuli, complementing the highly unbalanced input activity conveyed from the nose.

The PC is thought to create associative representations of the olfactory world and combine it with non-sensory information (Calu et al, 2007; Howard et al., 2009; Wiegand et al, 2011; Wilson and Sullivan, 2011 Poo et al., 2022). Circuits in the PC are likely to help normalize activity, creating equalized representations of diverse olfactory stimuli. Such normalization might also lead to concentration invariant representations, at least when firing rate metrics are used (Bolding and Franks, 2018). It has not been clear what information computed in the PC is passed on to the OB via feedback axons. Previous studies using monomolecular odorants that have imaged cortical axons have noted that the signals are broad and spatially non-local (Boyd et al., 2012; Otazu et al., 2015). Differences in activity in different brain states have also been reported, with larger odor-evoked responses in awake animals compared to anesthetized ones (Boyd et al., 2012). Intriguingly, task learning also appears to alter the activity patterns in cortical feedback (Wu et al., 2020; Chen et al., 2022; Trejo et al., 2023). Reducing the activity in cortical axons results in increased similarity of representations in mitral cells to different odors, suggesting that cortical axons ordinarily serve to decorrelate representations (Otazu et al., 2015; Chae et al., 2022). In this current study, we used a diverse set of odorants and created complex mixtures to mimic natural stimuli. By recording the responses of both OSNs and cortical feedback axons to the same set of diverse stimuli, we were able to directly compare their representations.

### *Selectivity and variability of cortical feedback activity*

We first characterized the odorant tuning of sensory neurons at the periphery and feedback projections to the OB, using a panel of monomolecular odorants. Consistent with the circuit architecture expansion from the OB to the PC we found that cortical feedback projections were more broadly tuned to monomolecular odorants than sensory inputs to the OB. Interestingly, however, for complex mixture stimuli, cortical boutons were on average more selective than OSNs (see below). This arises because complex mixtures with many components activate OSNs densely (despite widespread antagonistic interactions), but the responses of cortical boutons have similar sparsity for a wide range of stimuli. This feature means that the choice of stimuli could be important for comparing the responses of OSNs and PC neurons or axons - monomolecular odorants, which are widely used in experiments, may not be representative of the wide range of response densities that natural mixtures may evoke.

A key feature of cortical responses we observed is the significant trial-to-trial variability. Our imaging procedures necessitated a smaller number of repeats than those used in electrophysiological studies, but our estimates of variability match those reported previously for cell bodies of PC neurons (Bolding and Franks, 2017; Nagappan and Franks, 2021, Roland et al., 2017; Srinivasan et al 2023). This higher variability was not just due to waking conditions, since cortical bouton responses in anesthetized mice were also more variable

than OSN responses (**Supplementary Figure 2**). It remains unclear whether variability in stimulus encoding is a feature of cortical responsiveness to odorant stimuli, especially since this will be communicated back to the OB through descending projections. A recent study, which compared data from mammalian and insect third-order neurons, has proposed that stochasticity in responses may increase discriminability across odorant stimuli (Srinivasan et al 2023).

### *Representational similarity of odors in cortical feedback axons*

A widely proposed computational principle for many neural circuits and brain regions is that of pattern separation or pattern decorrelation (Leutgeb et al., 2007; McHugh et al., 2007; Sahay et al., 2011; Gschwend et al., 2015; Wilson 2009; Cayco-Gajic and Silver, 2019). In the olfactory system, this concept is applied in the context of decreasing the similarity of representations of distinct stimuli to allow for easier and more efficient decoding (Gschwend et al., 2015; Friedrich and Wiechert, 2014; Wilson, 2009). Odors activate overlapping sets of OSNs, and the similarity of their sensory representation is governed by the ligand-receptor binding properties, which depend partly on the physicochemical features of the ligands (Saito et al., 2009). The dispersed, unstructured projections from the OB to the PC will decrease the similarity of stimulus representations, but theoretical analysis predicts that some similarity can be preserved even when projections are random (Babadi and Sompolinski, 2014; Schaffer et al., 2018). That is, pairs of odors that are highly similar will have more similar representations in the PC than pairs of dissimilar odors. There is experimental evidence for this prediction, with a recent study reporting a relation between pairwise similarity in OB outputs and PC neurons (Pashkovski et al., 2020). However, it remains unclear how much pattern separation can still occur in the cortex, perhaps through experience and learning (Chapuis and Wilson, 2012).

The relatively large number of unique stimuli generated in our study using mixtures afforded a wide range of representational similarities in the OSNs. Remarkably, the pairwise similarities observed in cortical boutons were only slightly related to the similarities in the inputs to the brain (in fact, there was no relation at all for monomolecular odorants). This finding suggests that representations in feedback axons are altered much more than what might be predicted by feedforward random projections from OB to PC (Babadi and Sompolinski, 2014). For example, non-random associative connectivity within the PC (Haberly, 2001) could decorrelate signals further, removing any remaining correlations predicted theoretically. In addition, cortical connectivity, either through experience or developmental biases, could build additional correlations absent in the OB representation or selectively attenuate certain correlations (Pashkovskii et al., 2020). Our findings are also corroborated by recent work in insect brains, in which the similarity of representation in the output from the antennal lobe is not preserved in the mushroom body; instead, the representational similarity in the mushroom body seems to reflect covariances of odorant presence in natural odorant sources (Yang et al., 2023). While our data point to overall decorrelation, they do not address whether specific correlations are selectively enriched or built-in cortical feedback axons.

Our data also offer new insights into the computations underlying decorrelation of responses in the OB. Inhibiting feedback from the olfactory cortex has been shown to increase correlations in the representation of different monomolecular odors, suggesting that ordinarily, the activity of cortical feedback will serve to decorrelate representations (Otazu et al., 2015; Chae et al., 2022). Similarly, activation of raphe axons also decreases representational similarity (Kapoor et al., 2016). The general inference from these studies, even if implicit, is that feedback information is global and distributed and the selective recruitment of inhibition in the OB results in sparsening and decorrelation of M/T cell responses. Our data indicate that the feedback information is already significantly reformatted and decorrelated, which may reduce the demand for



more specific circuitry in the OB. Related experimental work in zebrafish, and some theoretical ideas developed from it, suggest that decorrelation cannot be accomplished by global rescaling and instead requires more structured connectivity (Wiechert et al., 2010; Friedrich and Wiechert, 2014). Cortical feedback axons carrying sparser decorrelated information, along with their plastic synapses (Gao and Strowbridge, 2009; Nissant et al., 2009), may facilitate pattern decorrelation in the OB.

#### *Olfactory cortical feedback axons carry normalized activity*

Our understanding of sensory encoding in the visual system has benefited greatly from the use of natural stimuli. The advances include explanations of the shape of receptive fields in early visual areas as arising from the statistics of natural images (Olshausen and Field, 1996) and sparse, decorrelated responses in the visual cortex elicited by natural images (Vinje and Gallant, 2000). Similar experiments in the olfactory system have been rare, in part because of the difficulty in presenting natural stimuli in a controlled and reliable manner. In one step towards more naturalistic stimuli, we used diverse mixtures of commonly used odorants. Since these stimuli will span a range of covariances, it allowed us to test whether cortical representation has signatures of transformations expected from efficient coding.

Several features we observed support the idea of a more efficient representation of mixture stimuli in cortical feedback. First, population responses of cortical boutons were equalized for different stimuli. While the fraction of OSNs responding increased with mixture complexity, this fraction remained nearly constant in cortical boutons (**Figure 5D**), significantly extending earlier work using monomolecular odorants or binary odorant mixtures and recording in the PC (Roland et al., 2017; Bolding and Franks 2017; Stettler and Axel, 2009). Recordings from anesthetized mice have indicated that responses of individual PC neurons to odor mixtures can be described by a normalization model, where increasing input density gets progressively more attenuated (Penker et al., 2020). In our studies, the activity generated by complex mixtures of odorants was massively normalized in cortical feedback axons arriving in the OB. This is in stark contrast to OSNs, where the density of activity increases with the progressive complexity of stimulus mixtures encountered, even though this increase is highly non-linear due to antagonistic interactions (Zak 2020; Xu et al., 2020; Pfister et al., 2020). It is likely that the circuit architecture in the PC with its feedforward and recurrent inhibition, serves to normalize and equalize responses.

A second signature of efficient coding is that the responses of individual cortical boutons were sparser than the responses of OSNs to the panel of 84 mixtures. Interestingly, when responses to single odorants are compared, cortical boutons appear to be denser. This feature might be simply due to the particular choice of odorants, and our ability to image only a small fraction of the entire OSN repertoire. Natural environments with mixtures of many odors are likely better approximated by our complex mixture stimuli, and those conditions will lead to sparsening of representations in cortical feedback axons.

#### *Nonmonotonic representations of odorant concentration in the feedback axons*

In contrast to the use of odorant mixtures, where antagonism contributes to the non-linear scaling of activity in sensory inputs, increasing odorant concentrations provides a mechanism to scale the activity of OSNs independent of antagonistic interactions. As concentration increases, the same population of OSNs is increasingly activated and new OSNs are recruited (Rubin and Katz, 1999) This contrasts with mixture stimulation, where more components can activate more OSNs, but without necessarily creating a gradual monotonic increase in the activity of OSNs.

A steady monotonic increase in the number and activity of OSNs as concentration increases might be predicted to result in increased activity of some cells in the PC. Previous studies have used the fraction of activated cells in the PC to argue for concentration invariant normalization, with a slight dependence on concentration (Roland et al., 2017; Bolding and Franks, 2018). In our study, we see that individual cortical boutons show strong non-monotonic dependence on odorant concentration (which cannot be construed as concentration invariant), even if the overall population response may be flatter. We also find that bouton representations of odorants increase in similarity with concentration. While this was hinted at in earlier studies (Otazu et al., 2015; Bolding and Franks, 2018), a systematic analysis has been lacking, as is a circuit-based explanation for such an observation.

We propose a simple cortical circuit model with activity-dependent global feedback inhibition that can explain the non-monotonic dependence of cortical activity on concentration. This model is meant to be a plausible explanation, and including more biological realism in the future can allow more features of the data to be explained - for example, different concentrations at which distinct cortical neurons can exhibit maximal responses, as well as a more gradual decline in response amplitudes at mid-range of concentrations. A caveat in our interpretation is that earlier work has noted that M/T cells in the OB can also exhibit non-monotonic concentration dependence (Chae et al., 2022). However, this phenomenon is likely to be due to the influence of cortical feedback, since inactivating it linearized M/T cell responses (Chae et al., 2022 Figure S8F). The effect is much stronger and more widespread in cortical boutons than in M/T cells, suggesting that this feature is not just simply inherited by PC neurons from the OB.

#### *Limitations of our study*

Our study has some limitations. First, all the functional measurements reported are from calcium indicators, which can mainly track slow variations in activity and cannot easily reveal timing or latency measures faster than ~100ms. However, a mitigating factor is that previous work has shown that average spike counts (or firing rate) carry much of the information in the PC (Miura et al 2012; Bolding and Franks, 2017). A second limitation, resulting from the design of the study, is that we imaged a subpopulation of PC neurons, only those with feedback projections to the OB. It is possible that other principal neurons in the PC have different properties. Previous work has shown that only deeper layer neurons send projections to the OB, and the superficial semilunar cells lack feedback projections (Mazo et al., 2017, Diodato et al., 2016). A recent study (Nagappan and Franks, 2021) indicated that semilunar and principal cells have many common properties, with only subtle differences in response tuning - therefore, our results are likely to generalize to other principal cells in PC. A third caveat is that the axonal and bouton activity could be influenced by local bulbar circuitry and may not faithfully represent somatic activity in PC neurons. For example, GABA<sub>B</sub> receptor-mediated presynaptic inhibition may suppress calcium responses locally (Mazo et al., 2016). Nevertheless, the net activity of cortical boutons, even if influenced by the bulbar environment, reflects the consequences for the postsynaptic targets within the OB and therefore functionally relevant. Finally, in this study, we examined responses in anesthetized as well as awake mice, but with no behavioral outcomes required. It is possible that task learning and engagement change response properties since mice are likely to be in a more attentive state (Fuentes et al., 2008; Wu et al., 2020; Trejo et al., 2023). It is unlikely, however, that OSN responses are very different, except for being modified by sniff dynamics.

#### *Conclusion*

The interaction between bottom-up and top-down information streams in the olfactory system is likely to aid in interpreting complex sensory scenes. Naturalistic odor environments contain dozens or more unique

odorants that must all be simultaneously parsed. Our studies demonstrate that cortical feedback maintains sparse odorant representations despite progressively dense sensory inputs, as likely to be encountered in natural environments. Whether sparse encoding, a hallmark of efficient neural processes, is maintained in cortical feedback as stimuli are assigned categorical relevance remains to be explored. Future studies using similar odorant delivery paradigms could explore how and if odorant representations in cortical projections are reformatted by learning and association.

## Methods

### *Experimental model and subject details*

Adult (> 8 weeks) C57Bl/6J or OMP-GCaMP3 mice of both sexes were used in this study. Mice were acquired from the Jackson Laboratory (C57Bl/6J) or breeding stocks at Harvard University (OMP-GCaMP3) and maintained within Harvard University's Biological Research Infrastructure for the duration of the study. All animals were between 20 and 30 g before surgery and singly housed following any surgical procedure. Animals were between three and six months old at the time of the experiments. All mice used in this study were housed in an inverted 12-hour light cycle at  $22 \pm 1$  °C at 30-70% humidity and fed *ad libitum*. All the experiments were performed in accordance with the guidelines set by the National Institutes of Health and approved by the Institutional Animal Care and Use Committee at Harvard University.

### *Viral injections*

All viruses used in this study were acquired from Addgene. AAV9.CAG.GCaMP6f.WPRE.SV40 (Addgene ID: 100836-AAV9) and AAV1-CAG-tdTomato (Addgene ID: 59462-AAV1). The two viruses were mixed in equal proportions prior to injection. Mice were anesthetized with an intraperitoneal injection of ketamine and xylazine (100 and 10 mg/kg, respectively) and the eyes were covered with petroleum jelly to keep them hydrated. Body temperature was maintained at 37 °C by a heating pad. The scalp was shaved and then opened with a scalpel blade. Two burr holes were then drilled above the anterior piriform cortex in each hemisphere. The coordinates for each of the injection sites are +1.2 or 1.6 mm AP relative to the intersection of the inferior cerebral vein and superior sagittal sinus, +2.8 mm ML relative to the intersection of the inferior cerebral vein and superior sagittal sinus, and -3.6 or -3.2 mm DV from the brain surface. Viruses were infused at a rate of 40 nL/min for a total volume of 200 nL at each site from a 33-gauge beveled-tip needle (Hamilton). The scalp was then closed with dissolvable sutures. Buprenorphine SR-Lab (1.0 mg/kg) was administered subcutaneously, and the mice were allowed to recover for at least two weeks before any additional procedures.

### *Confocal imaging*

Mice were deeply anesthetized with a ketamine/xylazine mixture and transcardially perfused with 20 mL of PBS (pH 7.4) first, followed by 30-50 mL of 4% paraformaldehyde in 0.1 M phosphate-buffered saline (pH 7.4). Brains were removed and cut into 70  $\mu$ m-thick sagittal sections using a vibratome (Leica). Slices were then washed and mounted for confocal imaging with DAPI mounting media and imaged with a confocal microscope (LSM 710 or 880, Zeiss).

### *OB craniotomy*

A craniotomy was performed to provide optical access to both OB. Mice were first anesthetized with an intraperitoneal injection of ketamine and xylazine (100 and 10 mg/kg, respectively), and the eyes were covered with petroleum jelly to keep them hydrated. Body temperature was maintained at 37 °C by a heating pad. The scalp was shaved and then opened with a scalpel blade. After thorough cleaning and drying, the

cranial bones over the OBs were then removed using a 3 mm diameter biopsy punch (Integra Miltex). The surface of the brain was cleared of debris. The surface of the brain was kept moist with artificial cerebrospinal fluid containing in mM (125 NaCl, 5 KCl, 10 Glucose, 10 HEPES, 2 CaCl<sub>2</sub>, and 2 MgSO<sub>4</sub> [pH 7.4]) and Gelfoam (Patterson Veterinary). Two 3 mm No. 1 glass coverslips (Warner) were glued together with optical adhesive (Norland Optical Adhesive 61) and adhered to the edges of the vacated cavity in the skull with Vetbond (3M). The posterior portion of the exposed skull was gently scratched with a blade, and a titanium custom-made headplate was glued (Loctite 404 Quick Set Adhesive) on the scratches. C&B-Metabond dental cement (Parkell, Inc.) was used to cover the headplate and form a well around the cranial window. After surgery, mice were treated with carprofen (6 mg/kg) and buprenorphine SR-Lab (1.0 mg/kg). Animals were allowed to recover for at least three days prior to acclimatization in the imaging room.

### *Bone thinning over the olfactory epithelium*

OMP-GCaMP3 mice were anesthetized using the same procedure and all pre-surgical methods through head plate implantation are the same as the craniotomy. The cranial bones over the olfactory epithelium, anterior to the frontonasal suture, and between the internasal and nasal-maxillary sutures were thinned with a dental drill and scalpel blade until transparent (Zak et al., 2020; Zak, 2022). The thinned area of the skull was then covered with cyanoacrylate adhesive (Loctite 404 Quick Set Adhesive) and a glass coverslip was implanted in the adhesive. Dental cement was then used to form a well over the thinned section of the skull. All animals were allowed to recover for at least three days before imaging experiments were initiated.

### *Multiphoton Imaging*

A custom-built two-photon microscope was used for *in vivo* imaging. Fluorophores were excited and imaged with a water immersion objective (20X, 0.95 NA, Olympus) at 920 nm using a Ti:Sapphire laser with dispersion compensation (Mai Tai HP, Spectra-Physics). Images were acquired at 16-bit resolution and 4-8 frames/s. The pixel size was 0.6  $\mu\text{m}$  for OSN somata and axon imaging. Fields of view ranged from 180  $\times$  180  $\mu\text{m}$  in the epithelium to 720  $\times$  720  $\mu\text{m}$  in the OB. The point-spread function of the microscope was measured to be 0.51  $\times$  0.48  $\times$  2.12  $\mu\text{m}$ . Image acquisition and scanning were controlled by custom-written software in LabView (National Instruments). Emitted light was routed through two dichroic mirrors (680dcxr, Chroma, and FF555-Di02, Semrock) and collected by a photomultiplier tube (R3896, Hamamatsu) using filters in the 500–550 nm range (FF01–525/50, Semrock).

### *Odor stimulation*

Monomolecular odorants (Sigma or Penta Manufacturing) were used as stimuli and delivered by custom-built 16-channel olfactometers controlled by custom-written software in LabView (Zak et al., 2018; Albeanu et al., 2018). For most experiments, the initial odorant concentration was 16% (v/v) in mineral oil, and further diluted 16 times with air. When using a concentration series, the initial odorant concentration was between 0.08% - 80% (v/v) in mineral oil and further diluted 16 times with air and the relative concentration was measured by a photoionization detector (PID; Aurora Scientific), then normalized to the largest detected signal for each odorant (**Supplemental Figure 6**). To create mixtures, air-phase dilution was used, and the total concentration of each odorant was held constant. For all experiments, the airflow to the animal was held constant at 100 mL/min, and odorants were injected into a carrier stream. Odorants were delivered 2–6 times each.

For experiments characterizing the odor tuning, the odor panel consisted of 1) Ethyl tiglate 2) Allyl tiglate 3) Hexyl tiglate 4) Methyl tiglate 5) Isopropyl tiglate 6) Citronellyl tiglate 7) Benzyl tiglate 8) Phenylethyl tiglate 9) Ethyl propionate 10) 2-Ethyl hexanal 11) Propyl acetate 12) 4-Allyl anisole 13) Ethyl valerate 14) Citronellal 15) Isobutyl propionate 16) Allyl butyrate. See **Supplementary Figure 7** for PID measurements. For experiments measuring complex mixture responses in cortical projections and the olfactory epithelium, odorants 1-16 were used from the panel above. Additional odorant information is available in **Table 1** and the composition of odorant mixtures is found in **Supplementary Table 1**.

### Data analysis

Images were processed using both custom and available MATLAB (Mathworks) scripts. Motion artifact compensation and denoising were done using NoRMcorre (Pnevmatikakis and Giovannucci, 2017). The CalmAn CNMF pipeline Field (Giovannucci et al., 2019) was used for bouton, epithelium, and axon imaging to select and demix ROIs. ROIs were further filtered by size and shape to remove merged cells. For signals obtained from glomeruli in the OB, custom scripts were written to manually select ROI boundaries (Zak et al., 2018). The mean  $\Delta F/F$  signal in the 5 s following odorant onset was used for measurements of neural activity in all experiments. To account for changes in respiration and anesthesia depth, correlated variability was corrected (Mathis et al., 2016). Thresholds for classifying responding ROIs were determined from a noise distribution of blank (no odorant) trials from which three standard deviations were used for responses. In each dataset, only ROIs with at least one significant odorant response were included for further analysis. Representational similarity between stimuli was estimated by calculating the Pearson correlation coefficient between population vectors that consisted of all ROIs that satisfied the thresholding criterion.

The expected fractions of boutons with only enhanced, only suppressed and mixed responses to all 16 odors were estimated from the overall response statistics obtained in **Figure 2B**. For each simulated bouton, 16 responses were randomly and independently drawn from the observed probability distribution (72.2% non-responsive, 12.4% enhanced, and 15.4% suppressed), and were classified as purely enhanced, purely suppressed, or mixed. Expected values and variance from 10,000 such simulations were obtained.

Sparseness measures were calculated as previously reported (Wallace et al., 2017). Population sparseness measures the fraction of elements (or cells) that are activated by a given odorant, with values near one indicating uniform activity across all elements and values near zero indicating a lack of activity in most elements:

$$PS_j = \frac{\left(\sum_{i=1}^n \frac{r_i}{n}\right)^2}{\sum_{i=1}^n \frac{r_i^2}{n}}$$

Where:  $n$  = the number of elements,  $r_i$  = the response of element  $A$  to odorant  $j$ .

Lifetime sparseness measures the extent to which a given element responds to different odorant stimuli. Values near one indicate all odorants uniformly activate a given element and values near zero indicate a high degree of odorant selectivity:

$$LS_i = \frac{\left(\sum_{j=1}^m \frac{r_j}{m}\right)^2}{\sum_{j=1}^m \frac{r_j^2}{m}}$$

Where:  $m$  = the number of odorants,  $r_j$  = response of element  $A$  to odorant  $j$ .

All statistical comparisons for imaging experiments were made as described in the text for each figure and values are given as mean + /- standard error of the mean.

#### OB-to-PC model

We consider a simplified model of connectivity between the OB and PC, which recapitulates the non-monotonic dose-response curves shown by the cortical neurons. We model the activity of two neuronal populations:  $N_g$  glomeruli in the OB and  $N_p$  cortical neurons that project back to the OB.

The activity of the bulbar neurons reflects the binding and activation of OSN receptors. The output of the  $i$ th glomerulus to an odor at concentration  $c$  is:

$$x_i(c) = \eta_i \frac{\kappa_i c}{1 + \kappa_i c},$$

where  $\kappa_i$  is the binding affinity of the odor to the receptors of the OSNs that project to the  $i$ th glomerulus and  $\eta_i$  is proportional to its corresponding activation efficacy. The logarithms of the binding affinities,  $\log \kappa_i$ 's, were drawn independently and identically distributed (i.i.d) from a normal distribution with mean zero and standard deviation 3 so that the affinities spanned approximately three orders of magnitude. The activation efficacies,  $\eta_i$ 's, are binary and drawn i.i.d from a Bernoulli distribution with probability 0.2, that is, an odor activates approximately 20% of the glomeruli at saturating concentrations.

The dynamics of cortical activity are determined by bulbar input and global, non-specific inhibition through a population of local interneurons. Inhibition from the interneuron turns on when the summed activity of the cortical neurons exceeds a certain threshold. The voltage dynamics of the  $j$ th cortical neuron ( $u_j$ ) after odor onset is given by:

$$\tau \frac{du_j}{dt} = -u_j - w_{inh} \sigma(\beta(v - v_{thr})) + \sum_{i=1}^{N_g} W_{ji} x_i,$$

where  $v$  is the voltage of the inhibitory interneuron whose output activity is sigmoidal:  $\sigma(\beta(v - v_{thr}))$ . This neuron (or, equivalently, a population of identical neurons) non-specifically inhibits all the cortical neurons with synaptic weight  $w_{inh}$ . The bulbar input to the cortex is determined by the  $N_p \times N_g$  sparse random matrix  $W$  whose entries are non-zero with probability 0.1 and the non-zero entries are drawn from a positive half-normal distribution with scale 0.5. This latter number is set so that the input into the cortical neurons at saturating concentrations has unit magnitude on average. Note that changing this value does not affect the results if  $w_{inh}$  is concomitantly scaled. A sparse  $W$  ensures that the bulbar input across the cortical population has a broad distribution and thereby produces a distinct cortical representation for each odor. The output activity  $y_j$  of the cortical neurons is rectified:  $y_j = u_j^+$ .  $\tau$  is an integration timescale, which we expect to be on the order of a hundred milliseconds.

The inhibitory interneuron receives and sums input from all cortical neurons. The voltage dynamics of the inhibitory interneuron is:

$$\tau \frac{dv}{dt} = -v + \sum_{j=1}^{N_p} y_j$$

We set  $w_{inh} = 1, \beta = 2, v_{thr} = 2000, N_g = 400, N_p = 5000$ .

To simulate heterogeneous inhibition (**Figure 7C**), we consider a population of 500 inhibitory interneurons in the PC. For each neuron, the three parameters,  $w_{inh}$ ,  $\beta$ , and  $v_{thr}$ , were set to the values in the single neuron case above and were each scaled by a random factor of  $1 + \varepsilon$  where  $\varepsilon$  is a normal random variable with mean zero and standard deviation 0.2.

#### *Data Availability*

The data supporting this study's findings are available from the corresponding author upon reasonable request.

#### *Code Availability*

The code used for analysis and figure generation of this study is available from the corresponding author upon reasonable request.

#### *Acknowledgments*

We thank Siddharth Jayakumar for his assistance with the confocal image collection, Ningjing Xia for thoughtful discussion on odorant mixtures, and all members of the Murthy and Zak Laboratories for helpful discussions. We also thank Bob Datta and Shyam Srinivasan for their helpful feedback on a draft of this manuscript.

#### *Declaration of Interests*

The authors declare no competing financial interests.

#### *Funding and Support*

This work was supported by NIH Grants K99/R00 DC017754 to JDZ and R01 DC011291 to VNM.

## References

1. Adefuin AM, Lindeman S, Reinert JK, Fukunaga I (2022) State-dependent representations of mixtures by the olfactory bulb. *Elife*. 11:e76882.
2. Albeanu DF, Provost AC, Agarwal P, Soucy ER, Zak JD, Murthy VN (2018) Olfactory marker protein (OMP) regulates formation and refinement of the olfactory glomerular map. *Nat Commun*. 9(1):5073
3. Apicella A, Yuan Q, Scanziani M, Isaacson JS (2010) Pyramidal cells in piriform cortex receive convergent input from distinct olfactory bulb glomeruli. *J Neurosci*. 30:14255-60.
4. Araneda RC, Kini AD, Firestein S (2000) The molecular receptive range of an odorant receptor. *Nat Neurosci*. 3:1248-55.
5. Atick JJ (1992) Could information theory provide an ecological theory of sensory processing? *Network: Computation in Neural Systems*. 3:2, 213-51.
6. Babadi B, Sompolinsky H (2014) Sparseness and expansion in sensory representations. *Neuron*. 83(5):1213-26.
7. Banerjee A, Marbach F, Anselmi F, Koh MS, Davis MB, Garcia da Silva P, Delevich K, Oyibo HK, Gupta P, Li B, Albeanu DF (2015) An interglomerular circuit gates glomerular output and implements gain control in the mouse olfactory bulb. *Neuron*. 87(1):193-207.
8. Barlow, H. B. in *Sensory Communication*. (ed. Rosenbluth, W. A.) 217-34 (MIT Press, Cambridge, Massachusetts, 1961)
9. Bekkers JM, Suzuki N (2013) Neurons and circuits for odor processing in the piriform cortex, *Trends in Neurosciences*, 36(7):429-38.
10. Bishop, C. M. *Neural Networks for Pattern Recognition*. (Clarendon Press. 1995)
11. Bolding KA, Franks KM (2017) Complementary codes for odor identity and intensity in olfactory cortex. *Elife*. 6:e22630.
12. Bolding KA, Franks KM (2018) Recurrent cortical circuits implement concentration-invariant odor coding. *Science*. 361(6407):eaat6904.
13. Bolding KA, Nagappan S, Han BX, Wang F, Franks KM (2020) Recurrent circuitry is required to stabilize piriform cortex odor representations across brain states. *Elife*. 9:1-23.
14. Boyd AM, Sturgill JF, Poo C, Isaacson JS (2012) Cortical feedback control of olfactory bulb circuits. *Neuron*. 76:1161-74.
15. Buck L, Axel R (1991) A novel multigene family may encode odorant receptors: a molecular basis for odor recognition. *Cell*. 65:175-87.
16. Burton SD (2017) Inhibitory circuits of the mammalian main olfactory bulb. *J Neurophysiol*. 118(4):2034-51.
17. Calu DJ, Roesch MR, Stalnaker TA, Schoenbaum G (2007) Associative encoding in posterior piriform cortex during odor discrimination and reversal learning. *Cereb Cortex*. 17(6):1342-9.
18. Cayco-Gajic NA, Silver RA (2019) Re-evaluating Circuit Mechanisms Underlying Pattern Separation. *Neuron*. 101(4):584-602.
19. Chapuis J, Wilson DA (2011) Bidirectional plasticity of cortical pattern recognition and behavioral sensory acuity. *Nat Neurosci*. 15(1):155-61.
20. Chae H, Banerjee A, Dussauze M, Albeanu DF (2022) Long-range functional loops in the mouse olfactory system and their roles in computing odor identity. *Neuron*. 110(23):3970-3985.e7.
21. Chen Z, Padmanabhan K (2022) Top-down feedback enables flexible coding strategies in the olfactory cortex. *Cell Rep*. 38(12):110545.



22. Cleland TA, Linster C (2005) Computation in the olfactory system. *Chem Senses*. 30(9):801-13.
23. Davison IG, Ehlers MD (2011) Neural circuit mechanisms for pattern detection and feature combination in olfactory cortex. *Neuron*. 70:82-94.
24. Diodato A, Ruinart de Brimont M, Yim YS, Derian N, Perrin S, Pouch J, Klatzmann D, Garel S, Choi GB, Fleischmann A (2016) Molecular signatures of neural connectivity in the olfactory cortex. *Nat Commun*. 7:12238.
25. Fletcher ML, Masurkar AV, Xing J, Imamura F, Xiong W, Nagayama S, Mutoh H, Greer CA, Knöpfel T, Chen WR (2009) Optical imaging of postsynaptic odor representation in the glomerular layer of the mouse olfactory bulb. *J. Neurophysiol*. 102:817-30.
26. Friedrich RW, Wiechert MT (2014) Neuronal circuits and computations: pattern decorrelation in the olfactory bulb. *FEBS Lett*. 588(15):2504-13.
27. Fuentes RA, Aguilar MI, Aylwin ML, Maldonado PE (2008) Neuronal activity of mitral-tufted cells in awake rats during passive and active odorant stimulation. *J Neurophysiol*. 100(1):422-30.
28. Gao Y, Strowbridge BW (2009) Long-term plasticity of excitatory inputs to granule cells in the rat olfactory bulb. *Nat Neurosci*. 12(6):731-3.
29. Giovannucci A, Friedrich J, Gunn P, Kalfon J, Brown BL, Koay SA, Taxidis J, Najafi F, Gauthier JL, Zhou P, Khakh BS, Tank DW, Chklovskii DB, Pnevmatikakis EA (2019) CalmAn an open source tool for scalable calcium imaging data analysis. *eLife*. 8:e38173.
30. Gschwend O, Abraham NM, Lagier S, Begnaud F, Rodriguez I, Carleton A (2015) Neuronal pattern separation in the olfactory bulb improves odor discrimination learning. *Nat Neurosci*. 18(10):1474-1482.
31. Haberly LB, Price JL (1977) The axonal projection patterns of the mitral and tufted cells of the olfactory bulb in the rat. *Brain Res*. 129:152-7.
32. Haberly LB (2001) Parallel-distributed processing in olfactory cortex: new insights from morphological and physiological analysis of neuronal circuitry. *Chem Senses*. 26(5):551-76.
33. Howard JD, Plailly J, Grueschow M, Haynes JD, Gottfried JA (2009) Odor quality coding and categorization in human posterior piriform cortex. *Nat Neurosci*. 12(7):932-8.
34. Inagaki S, Iwata R, Iwamoto M, Imai T (2020) Widespread inhibition, antagonism, and synergy in mouse olfactory sensory neurons in vivo. *Cell Rep*. 31:107814.
35. Iurilli G, Datta SR (2017) Population coding in an innately relevant olfactory area. *Neuron*. 93(5):1180-1197.e7.
36. Kapoor V, Provost AC, Agarwal P, Murthy VN (2016) Activation of raphe nuclei triggers rapid and distinct effects on parallel olfactory bulb output channels. *Nat Neurosci*. 19(2):271-82.
37. Kato HK, Chu MW, Isaacson JS, Komiyama T (2012) Dynamic sensory representations in the olfactory bulb: modulation by wakefulness and experience. *Neuron*. 76:962-75.
38. Lin DY, Shea SD, Katz LC (2006) Representation of natural stimuli in the rodent main olfactory bulb. *Neuron*. 50:937-49.
39. Leutgeb JK, Leutgeb S, Moser MB, Moser EI (2007) Pattern separation in the dentate gyrus and CA3 of the hippocampus. *Science*. 315(5814):961-6.
40. Malnic B, Hirono J, Sato T, Buck LB (1999) Combinatorial receptor codes for odors. *Cell*. 96:713-23.
41. Markopoulos F, Rokni D, Gire DH, Murthy VN (2012) Functional properties of cortical feedback projections to the olfactory bulb. *Neuron*. 76:1175-88.
42. Mathis A, Rokni D, Kapoor V, Bethge M, Murthy VN (2016) Reading out olfactory receptors: feedforward circuits detect odors in mixtures without demixing. *Neuron*. 91:1110-23.

43. Mazo C, Lepousez G, Nissant A, Valley MT, Lledo PM (2016) GABAB Receptors Tune Cortical Feedback to the Olfactory Bulb. *J Neurosci.* 36(32):8289-304.
44. Mazo C, Grimaud J, Shima Y, Murthy VN, Lau CG (2017) Distinct projection patterns of different classes of layer 2 principal neurons in the olfactory cortex. *Sci Rep.* 7(1):8282.
45. McHugh TJ, Jones MW, Quinn JJ, Balthasar N, Coppari R, Elmquist JK, Lowell BB, Fanselow MS, Wilson MA, Tonegawa S (2007) Dentate gyrus NMDA receptors mediate rapid pattern separation in the hippocampal network. *Science.* 317(5834):94-9.
46. Miura K, Mainen ZF, Uchida N (2012) Odor representations in olfactory cortex: distributed rate coding and decorrelated population activity. *Neuron.* 74(6):1087-98.
47. Mombaerts P, Wang F, Dulac C, Chao SK, Nemes A, Mendelsohn M, Edmondson J, Axel R (1996) Visualizing an olfactory sensory map. *Cell.* 87(4):675-86.
48. Nagappan S, Franks KM (2021) Parallel processing by distinct classes of principal neurons in the olfactory cortex. *Elife.* 10:e73668.
49. Nissant A, Bardy C, Katagiri H, Murray K, Lledo PM (2009) Adult neurogenesis promotes synaptic plasticity in the olfactory bulb. *Nat Neurosci.* 12(6):728-30.
50. Olshausen BA, Field DJ (1996) Emergence of simple-cell receptive field properties by learning a sparse code for natural images. *Nature.* 381:607-9.
51. Otazu GH, Chae H, Davis MB, Albeanu DF (2015) Cortical feedback decorrelates olfactory bulb output in awake mice. *Neuron.* 86:1461-77.
52. Pashkovski SL, Iurilli G, Brann D, Chicharro D, Drummey K, Franks KM, Panzeri S, Datta SR (2020) Structure and flexibility in cortical representations of odour space. *Nature.* 583(7815):253-58.
53. Penker S, Licht T, Hofer KT, Rokni D (2020) Mixture coding and segmentation in the anterior piriform cortex. *Front Syst Neurosci.* 14:604718.
54. Pfister P, Smith BC, Evans BJ, Brann JH, Trimmer C, Sheikh M, Arroyave R, Reddy G, Jeong HY, Raps DA, Peterlin Z, Vergassola M, Rogers ME (2020) Odorant receptor inhibition is fundamental to odor encoding. *Curr Biol.* 30(13):2574-2587.e6.
55. Pnevmatikakis EA, Giovannucci A (2017) NoRMCorre: An online algorithm for piecewise rigid motion correction of calcium imaging data. *J. Neurosci. Methods.* 291:83-94.
56. Pnevmatikakis EA (2018) Analysis pipelines for calcium imaging data. *Current Opinion in Neurobiology.* 55:15-21.
57. Poo C, Agarwal G, Bonacchi N, Mainen ZF (2022) Spatial maps in piriform cortex during olfactory navigation. *Nature.* 601(7894):595-99.
58. Pressler RT, Strowbridge BW (2017) Direct recording of dendrodendritic excitation in the olfactory bulb: Divergent properties of local and external glutamatergic inputs govern synaptic integration in granule cells. *J Neurosci.* 37:2033-7.
59. Ressler KJ, Sullivan SL, Buck LB (1994) Information coding in the olfactory system: evidence for a stereotyped and highly organized epitope map in the olfactory bulb. *Cell.* 79(7):1245-55.
60. Rinberg D, Koulakov A, Gelperin A (2006) Sparse odor coding in awake behaving mice *J Neurosci.* 26:8857-65.
61. Rokni D, Hemmelder V, Kapoor V, Murthy VN (2014) An olfactory cocktail party: figure-ground segregation of odorants in rodents. *Nat. Neurosci.* 17:1225-32.
62. Roland B, Deneux T, Franks KM, Bathellier B, Fleischmann A (2017) Odor identity coding by distributed ensembles of neurons in the mouse olfactory cortex. *Elife.* 6:e26337.

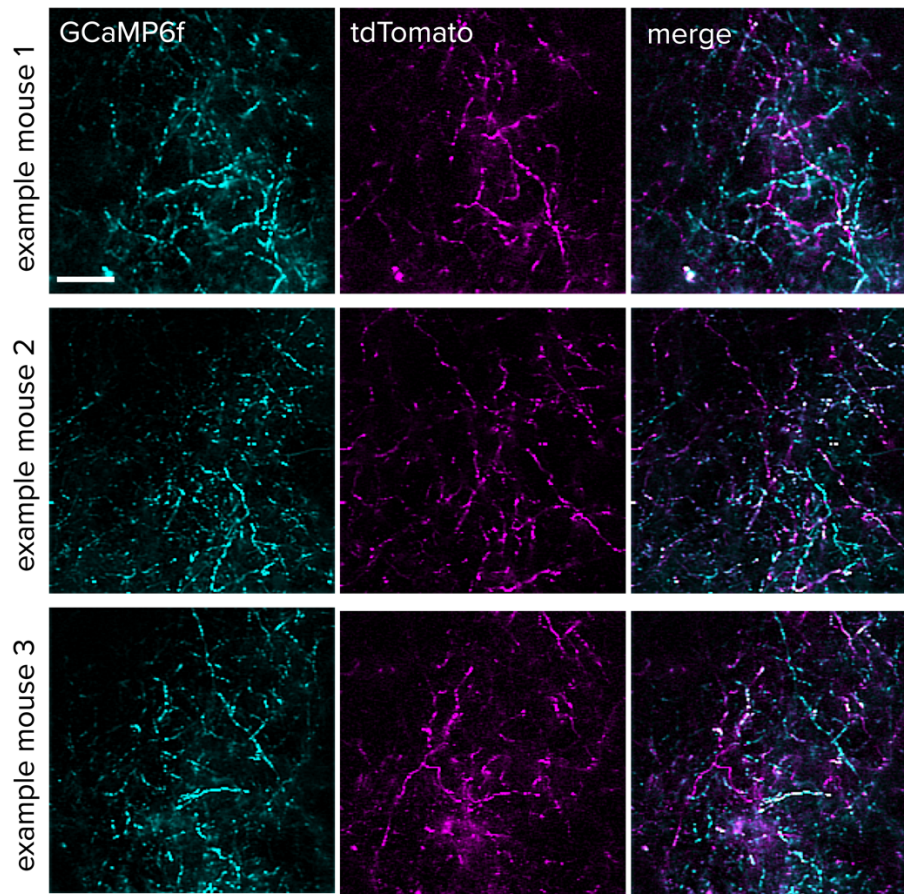
63. Rospars JP, Lansky P, Chaput M, Duchamp-Viret P (2008) Competitive and noncompetitive odorant interactions in the early neural coding of odorant mixtures. *J Neurosci.* 28:2659-66.
64. Rospars JP, Lánský P, Duchamp-Viret P, Duchamp A (2000) Spiking frequency versus odorant concentration in olfactory receptor neurons. *BioSystems.* 58:133-41.
65. Rubin BD, Katz LC (1999) Optical imaging of odorant representations in the mammalian olfactory bulb. *Neuron.* 23(3):499-511.
66. Sahay A, Wilson DA, Hen R (2011) Pattern separation: a common function for new neurons in hippocampus and olfactory bulb. *Neuron.* 70(4):582-8.
67. Saito H, Chi Q, Zhuang H, Matsunami H, Mainland JD (2009) Odor coding by a mammalian receptor repertoire. *Sci Signal.* 2(60):ra9.
68. Schaffer ES, Stettler DD, Kato D, Choi GB, Axel R, Abbott LF (2018) Odor perception on the two sides of the brain: consistency despite randomness. *Neuron.* 98(4):736-42.e3.
69. Smith EC, Lewicki MS (2006) Efficient auditory coding. *Nature.* 439(7079):978-82.
70. Sosulski DL, Bloom ML, Cutforth T, Axel R, Datta SR (2011). Distinct representations of olfactory information in different cortical centres. *Nature.* 472, 213-16.
71. Srinivasan S, Daste S, Modi M, Turner G, Fleischmann A, Navlakha S. (2023) Stochastic coding: a conserved feature of odor representations and its implications for odor discrimination. *PLoS Biology* (in press).
72. Stettler DD, Axel R (2009) Representations of odor in the piriform cortex. *Neuron.* 63:854-64.
73. Teng B, Wilson CE, Tu YH, Joshi NR, Kinnamon SC, Liman ER (2019) Cellular and neural responses to sour stimuli require the proton channel Otop1. *Curr. Biol.* 29:3647-56.e5.
74. Trejo DH, Ciuparu A, da Silva PG, Velasquez CM, Rebouillat B, Gross MD, Davis MB, Muresan RC, Albeanu DF (2023) Fast updating feedback from piriform cortex to the olfactory bulb relays multimodal reward contingency signals during rule-reversal. *bioRxiv* 2023.09.12.557267
75. Vassar R, Chao SK, Sitcheran R, Nuñez JM, Vosshall LB, Axel R. (1994) Topographic organization of sensory projections to the olfactory bulb. *Cell.* 79(6):981-91.
76. Vicente MI, Mainen ZF (2011) Convergence in the piriform cortex. *Neuron* 70:1-2.
77. Vinje WE, Gallant JL. (2000) Sparse coding and decorrelation in primary visual cortex during natural vision. *Science.* 287(5456):1273-6.
78. Wachowiak M, Shipley MT (2006) Coding and synaptic processing of sensory information in the glomerular layer of the olfactory bulb. *Semin Cell Dev Biol.* 17:411-23.
79. Wallace JL, Wienisch M, Murthy VN (2017) Development and refinement of functional properties of adult-born neurons. *Neuron.* 96:883-96.e7.
80. Wanner AA, Friedrich RW (2020) Whitening of odor representations by the wiring diagram of the olfactory bulb. *Nat Neurosci.* 23(3):433-42.
81. Wen B, Wang GI, Dean I, Delgutte B (2009) Dynamic range adaptation to sound level statistics in the auditory nerve. *J Neurosci.* 29:13797-808.
82. Wiechert MT, Judkewitz B, Riecke H, Friedrich RW (2010) Mechanisms of pattern decorrelation by recurrent neuronal circuits. *Nat Neurosci.* 2010 13(8):1003-10.
83. Wiegand HF, Beed P, Bendels MH, Leibold C, Schmitz D, Jochenning FW (2011) Complementary sensory and associative microcircuitry in primary olfactory cortex. *J Neurosci.* 31(34):12149-58.
84. Wilson RI, Mainen ZF (2006) Early events in olfactory processing. *Annu Rev Neurosci.* 29:163-201.
85. Wilson DA (2009) Pattern separation and completion in olfaction. *Ann N Y Acad Sci.* 2009 1170:306-12.

86. Wilson DA, Sullivan RM (2011) Cortical processing of odor objects. *Neuron*. 72(4):506-19.
87. Wu A, Yu B, Chen Q, Matthews GA, Lu C, Campbell E, Tye KM, Komiyama T (2020) Context-dependent plasticity of adult-born neurons instructed by cortical feedback. *Science Advances*. 6(42):eabc8319.
88. Xu L, Li W, Voleti V, Zou D-J, Hillman EMC, Firestein S (2020) Widespread receptor-driven modulation in peripheral olfactory coding. *Science*. 368:eaz5390.
89. Yang JY, O'Connell TF, Hsu WM, Bauer MS, Dylla KV, Sharpee TO, Hong EJ (2023) Restructuring of olfactory representations in the fly brain around odor relationships in natural sources. *bioRxiv*. 16:2023.02.15.528627.
90. Zak JD (2022) Longitudinal imaging of individual olfactory sensory neurons in situ. *Front Cell Neurosci*. 16:946816.
91. Zak JD, Grimaud J, Li RC, Lin CC, Murthy VN (2018) Calcium-activated chloride channels clamp odor-evoked spike activity in olfactory receptor neurons. *Sci Rep*. 8:1-13.
92. Zak JD, Reddy G, Vergassola M, Murthy VN (2020) Antagonistic odor interactions in olfactory sensory neurons are widespread in freely breathing mice. *Nat Commun*. 11:1-12.
93. Zelano C, Bensafi M, Porter J, Mainland J, Johnson B, Bremner E, Telles C, Khan R, Sobel N (2005) Attentional modulation in human primary olfactory cortex. *Nat Neurosci*. 8:114-20.
94. Zelano C, Mohanty A, Gottfried JA (2011) Olfactory predictive codes and stimulus templates in piriform cortex. *Neuron*. 72(1):178-87.

## Supplemental Figures

### Supplemental Figure 1

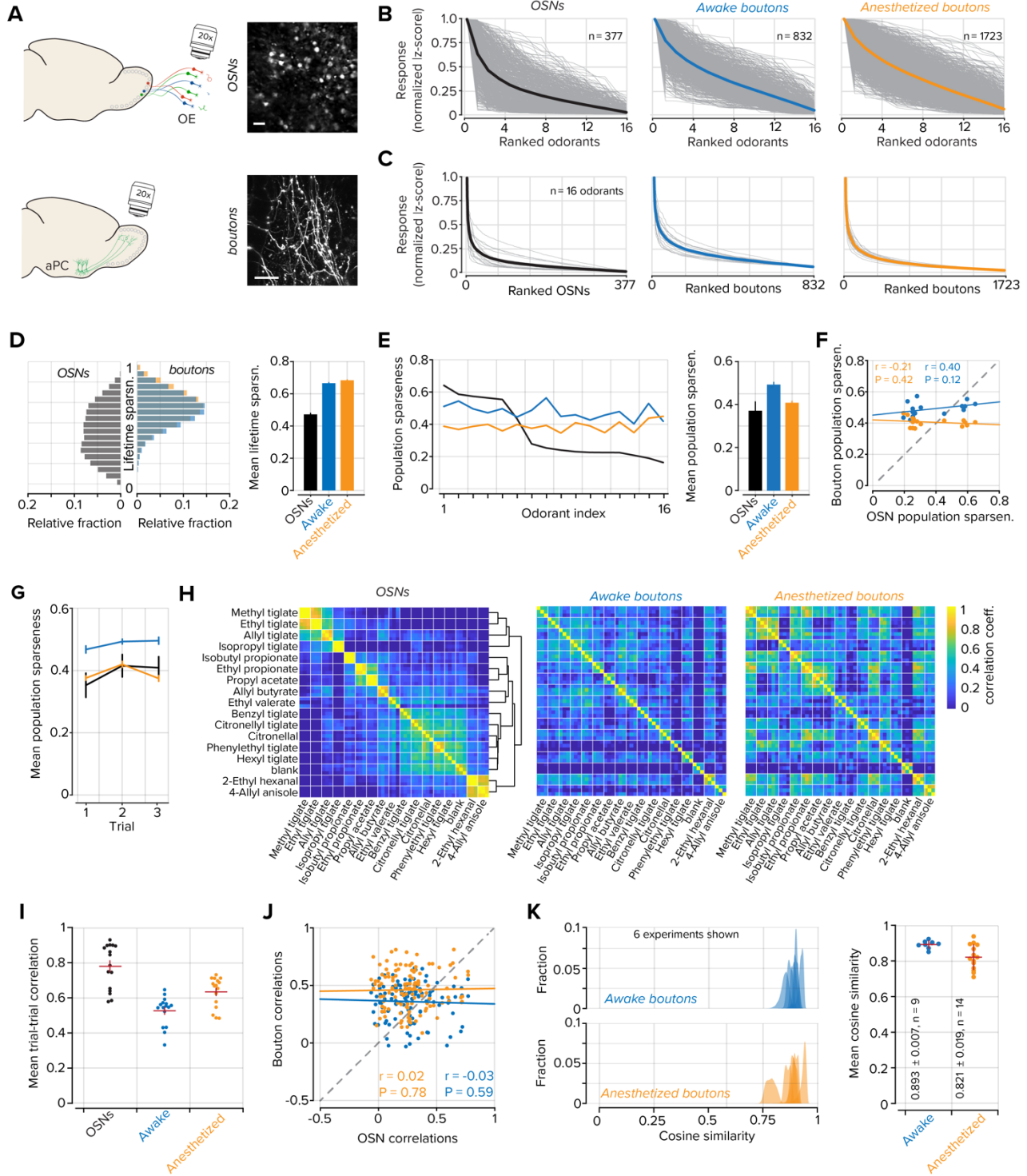
axon projections from the aPC imaged in OB granule cell layer



#### ***Co-labeled cortical axons in the olfactory bulb.***

Example imaging fields through a cranial window from three live mice. Cortical projections to the OB are labeled with GCaMP6f (*left*) and tdTomato (*middle*). Merged image at the right. scale bar = 20  $\mu$ m.

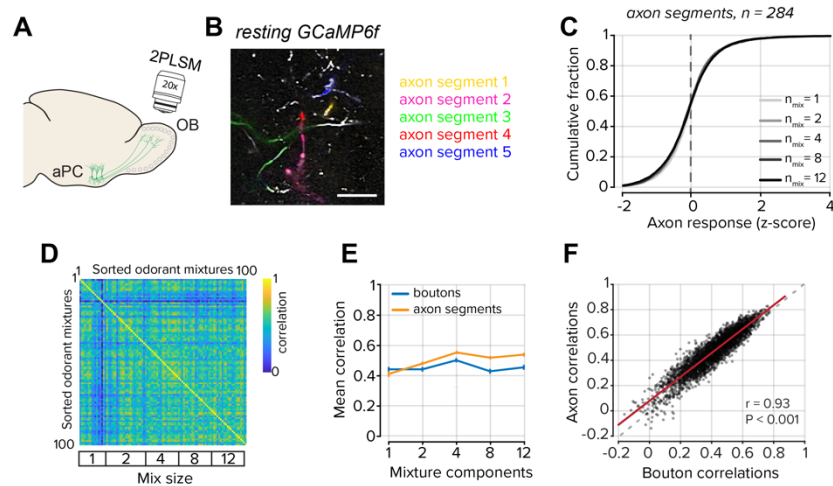
## Supplemental Figure 2



### **Odorant tuning in awake and anesthetized boutons.**

**A.** *Top*, example images of GCaMP3 expressing OSNs in the olfactory epithelium, scale bar = 20  $\mu\text{m}$ . *Bottom*, GCaMP6f expressing cortical projections to the OB, scale bar = 20  $\mu\text{m}$ . **B.** Normalized and ranked responses to 16 odorants in OSNs (black;  $n = 377$ ), cortical projections in awake mice (blue,  $n = 832$ ), and in anesthetized mice (orange;  $n = 1723$ ). Each tuning curve is independently sorted and ranked. Gray lines represent individual ROIs and thick colored lines represent the mean of all ROIs. **C.** Normalized and ranked responses of each OSN, cortical projection in awake mice, and anesthetized mice for each of the 16 odorants. Gray lines represent individual odorants and thick colored lines represent the mean of all odorants. **D.** *Left*, Distributions of lifetime sparseness measured in OSNs (black), cortical projections in awake mice (blue), and anesthetized mice (orange). *Right*, mean lifetime sparseness was measured in OSNs (black;  $0.24 \pm 0.01$ ), cortical projections in awake mice (blue;  $0.36 \pm 0.01$ ), and anesthetized mice (orange;  $0.47 \pm 0.01$ ).  $P < 0.001$ , all comparisons; Kolmogorov-Smirnov test. Error bars represent s.e.m. **E.** *Left*, population sparseness for each of 16 odorants sorted to OSN values. *Right*, mean population sparseness for all odorants, ( $0.08 \pm 0.02$  OSNs,  $0.02 \pm 0.01$  awake boutons,  $0.11 \pm 0.01$  anesthetized boutons;  $P < 0.001$ ; Kruskal-Wallis test). Error bars represent s.e.m. **F.** Scatter plot of the relationship between OSN population sparseness and bouton population sparseness in awake or anesthetized mice (anesthetized boutons to OSNs  $r = 0.27$ ;  $P = 0.31$ ; awake boutons to OSNs  $r = 0.13$ ;  $P = 0.63$ ). **G.** Mean population sparseness for each of three trials. Error bars represent s.e.m. **H.** Odorant-odorant correlations in OSNs, awake boutons, and anesthetized boutons. Individual odorants are bounded by white lines and each odorant contains three trials. Hierarchical clustering was used to group similar odorants in OSNs and the clusters were then used to group datasets in boutons. **I.** Variability within trials of the same odorants in OSNs and awake or anesthetized boutons.  $P < 0.001$  Kruskal-Wallis test. The horizontal red bar denotes the mean and the vertical red bars represent s.e.m. **J.** Scatter plot of the relationship between odorant-odorant correlations in OSNs and awake or anesthetized boutons (awake boutons to OSNs  $r = -0.03$ ;  $P = 0.59$ ; anesthetized boutons to OSNs  $r = 0.02$ ;  $P = 0.78$ ). **K.** Decreased correlations in awake boutons are not the product of motion artifacts. *Left*, distributions of the cosine similarity between a template image and each frame in an imaging session from six example experiments in awake and anesthetized preparations. *Right*, Summary data of all imaging sessions. The horizontal red bar denotes the mean and the vertical red bars represent s.e.m.

### Supplemental Figure 3

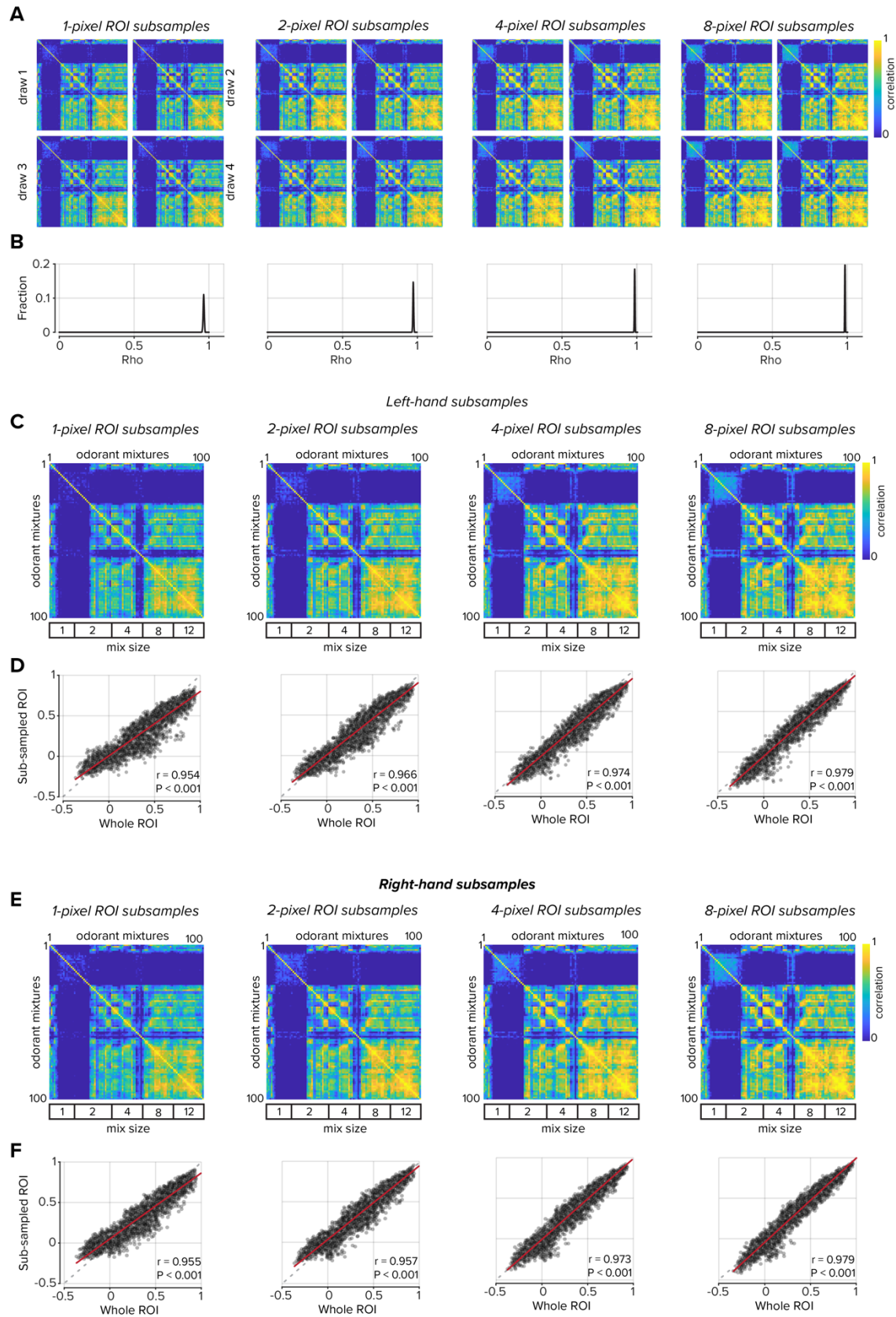


#### Odorant mixture correlations in axon segments.

**A.** Cortical axons expressing GCaMP6f were imaged in the OB through cranial windows. **B.** GCaMP6f expressing cortical projections to the OB. Identified axon segments are labeled in colors. scale bar = 20  $\mu\text{m}$ . **C.** Distributions of axon segment responses to odorant mixtures of increasing size. Color shade corresponds to the mixture size. **D.** Correlation matrix of mixture-mixture relationships in axon segments. **E.** Plot of the mean correlation of all mixtures at each mixture complexity, axon segments in orange, boutons from **Figure 5** in blue. Error bars represent s.e.m. **F.** Scatter plot of the relationship between mixture-mixture correlations measured in axon segments and boutons ( $r = 0.93$ ;  $P < 0.001$ ).



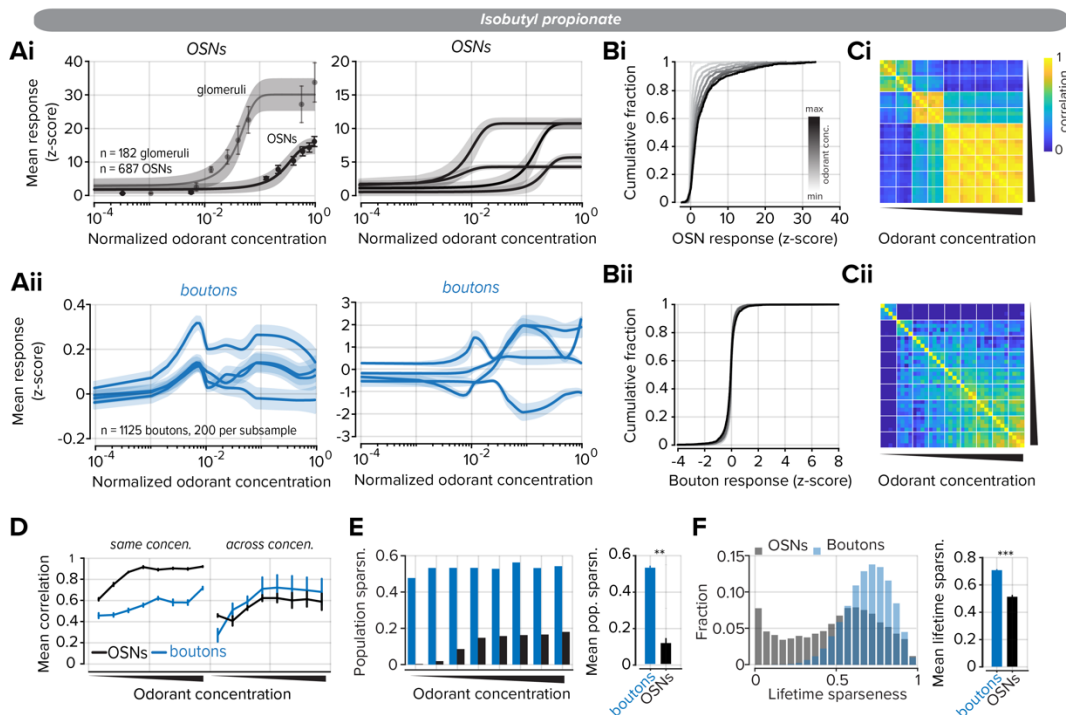
### Supplemental Figure 4



***Odorant mixture correlations in subsampled OSN regions of interest.***

**A.** Each OSN's ROI was subsampled to randomly select one, two, four, or eight pixels. Mixture-mixture correlations were then computed as in **Figure 6A**. Four example draws are shown for each subsample. **B.** Each subsample size was drawn 500 times and the mixture-mixture correlations of each subsample were then compared to the whole-ROI data (**Figure 6A**). Distributions of rho values from linear regressions are plotted. For each regression,  $P < 0.001$ . A single pixel from each OSN was sufficient to reproduce the whole-ROI correlation matrix. **C.** A second subsampling approach was used to select the one, two, four, or eight most pixels at the whole-ROI left-hand boundary. Mixture-mixture correlations were then computed. **D.** Comparison of the subsamples of each size and the whole-ROI mixture-mixture correlations. **E-F.** Same as parts C-D using left-hand subsamples.

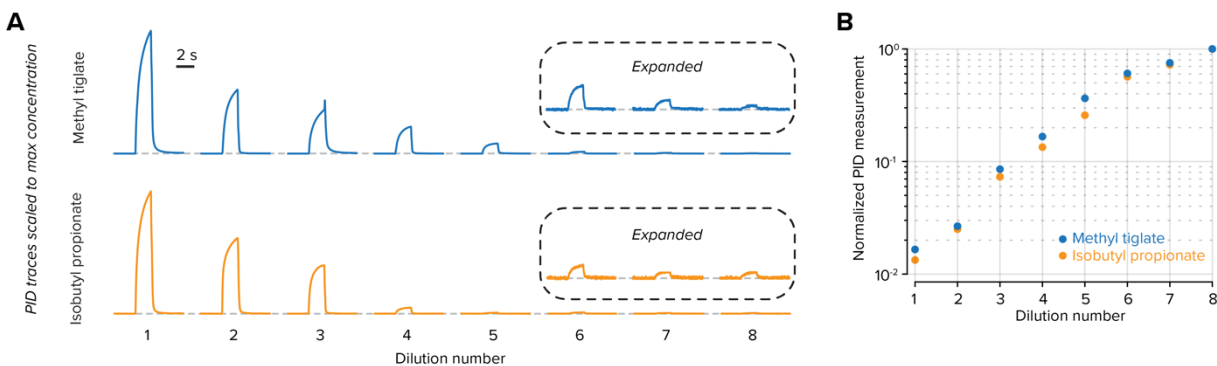
## Supplemental Figure 5



### **Nonmonotonic concentration responses in cortical boutons in response to the odorant Isobutyl propionate.**

**Ai. Left**, odorant concentration responses were measured at OSN somata in the OE and their axon terminals within the glomerular layer. Error expressed as s.e.m on individual data points and shaded 95% confidence interval for the sigmoidal fit. **Right**, four example OSN responses. **Aii. Left**, odorant concentration responses were measured at cortical boutons in the OB. Four traces show subsamples selected from 200 boutons each. The data were fitted with an Akima piecewise cubic Hermite interpolation. The shaded area represents the confidence interval. **Right**, four examples of individual bouton responses. **B**. Distributions of OSN (**Bi**) and bouton (**Bii**) responses to increasing odorant concentration. Color shade corresponds to the odorant concentration. **C**. Correlation matrix of odorant responses to increasing odorant concentration in OSNs (**Ci**) and boutons (**Cii**). White lines bound concentrations and each concentration contains four trials. **D. Left**, OSN, and bouton correlations between the same odorant concentration trials. **Right**, OSN and bouton correlations across concentrations. **E. Left**, population sparseness at each odorant concentration. **Right**, summary data of mean population sparseness for all concentrations. Error bars represent s.e.m. **F. Left**, Distributions of lifetime sparseness measured for all concentrations. **Right**, summary data of mean lifetime sparseness. Error bars represent s.e.m. \*\* denotes  $P < 0.01$ , \*\*\* denotes  $P < 0.001$ .

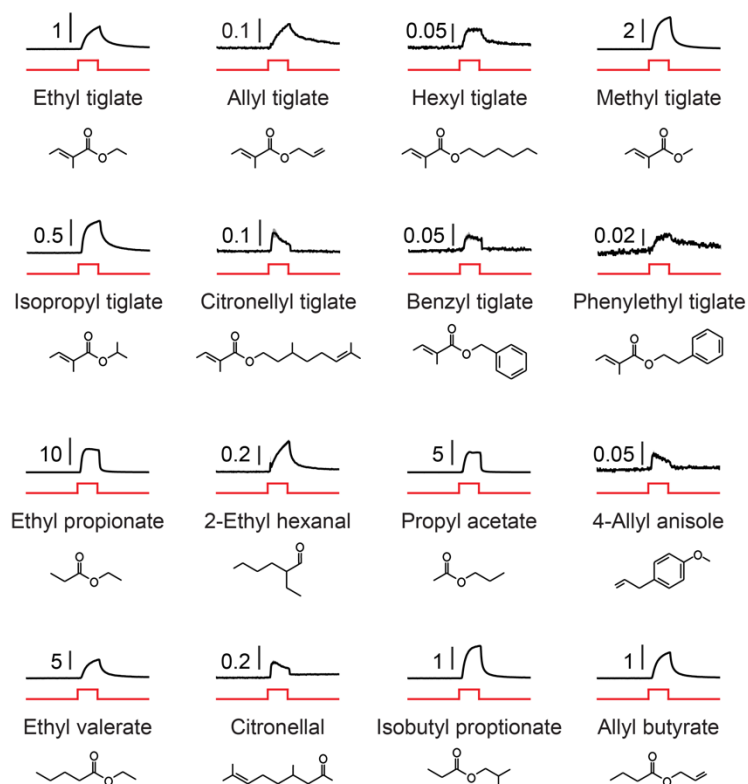
## Supplemental Figure 6



### Photoionization detector (PID) traces for odorant concentrations.

**A.** PID traces for concentrations of Methyl tiglate (**Figure 6**) and Isobutyl propionate (**Supplemental Figure 5**) at eight v/v dilutions (see Methods). Odorants were delivered for 2 s. Expanded traces show PID signals at the lowest concentrations. **B.** For each v/v dilution, the area under the PID trace was measured and plotted relative to the highest concentration.

### Supplemental Figure 7



#### Photoionization detector (PID) traces for odorants in Table 1

PID traces of all odorants used in tuning and mixture experiments in black (mean of 5 trials), voltage command to olfactometer in red. The molecular shape of each odorant is below the corresponding traces. Scale bar units are volts.

**Supplemental Table 1**

<b>mixture size</b>	<b>mixture component indices</b>	<b>mixture size</b>	<b>mixture component indices</b>
2	13,15	8	2,5,6,7,10,12,14,15
2	5,12	8	1,2,6,7,8,10,11,14
2	4,8	8	1,4,5,9,10,11,12,15
2	1,15	8	1,4,5,6,9,10,11,16
2	1,12	8	1,6,10,11,12,13,14,16
2	2,3	8	1,4,6,8,9,10,12,14
2	9,11	8	1,2,3,4,7,9,11,15
2	1,4	8	5,6,7,8,10,11,14,16
2	6,9	8	1,2,3,5,6,8,11,15
2	4,13	8	1,6,8,10,12,13,14,16
2	3,4	8	1,3,4,5,9,10,12,16
2	13,14	8	2,3,6,7,9,12,13,15
2	9,15	8	1,4,9,10,11,14,15,16
2	3,11	8	1,4,5,8,10,11,12,14
2	7,12	8	3,5,6,9,10,13,15,16
2	5,15	8	1,2,3,4,9,11,13,16
2	8,15	8	2,3,4,7,8,10,11,15
2	12,14	8	2,3,4,5,6,12,14,16
2	2,6	8	1,4,5,7,12,14,15,16
2	1,7	8	2,3,5,6,9,10,11,16
2	10,16	12	2,4,7,8,9,10,11,12,13,14,15,16
2	3,12	12	2,3,4,6,7,8,9,10,11,12,14,16
2	1,16	12	1,3,4,5,6,7,9,10,11,13,14,15
2	4,11	12	1,3,4,6,7,8,9,10,12,13,15,16
4	3,4,10,11	12	1,2,3,4,6,8,9,10,12,14,15,16
4	1,2,4,6	12	1,2,3,5,8,9,11,12,13,14,15,16
4	4,5,6,14	12	1,2,3,4,6,9,11,12,13,14,15,16
4	4,6,10,13	12	1,3,4,5,6,7,8,10,11,12,13,15
4	6,13,14,15	12	1,4,5,6,7,9,11,12,13,14,15,16
4	1,5,6,8	12	2,3,5,6,7,8,9,10,11,12,13,16
4	3,7,10,14	12	1,2,3,4,6,7,8,9,11,12,14,15
4	9,10,11,12	12	1,2,3,4,5,7,8,9,11,12,14,15
4	2,3,4,14	12	1,2,3,4,5,6,7,8,11,12,13,15
4	3,10,14,15	12	3,4,6,7,9,10,11,12,13,14,15,16
4	2,8,15,16	12	1,3,5,6,7,9,10,11,12,13,14,15
4	7,8,11,12	12	1,2,3,5,6,8,10,12,13,14,15,16
4	2,4,12,14	12	1,2,5,6,7,8,9,10,12,14,15,16
4	5,6,9,11	12	2,3,4,5,7,8,10,11,12,13,15,16
4	9,11,12,16	12	3,4,6,7,8,9,10,11,12,13,14,15
4	1,2,3,12	12	3,5,6,7,8,9,11,12,13,14,15,16
4	8,12,14,15		
4	3,4,8,9		
4	2,9,10,11		
4	3,8,9,13		

**Odorant mixture compositions**

Odorant mixture compositions Related to Figures 4 & 5. Odorant component indices are consistent with Table 1.